Biophysical Modeling of Capacitive Electro-Quasistatic Human Body Powering

Lingke Ding, *Student Member, IEEE*, Arunashish Datta, *Student Member, IEEE* and Shreyas Sen, *Senior Member, IEEE*

***Abstract*— The increasing demand for wearables necessitates efficient energy harvesting and wireless power transfer solutions. Capacitive Electro-Quasistatic Human Body Powering (EQS-HBP) is a promising technology for wirelessly powering on-body devices, offering enhanced received power (P_{rx}) with full-body coverage. Unlike EQS Human Body Communication (EQS-HBC), which optimizes channel capacity, EQS-HBP focuses on maximizing P_{rx}, requiring a distinct biophysical model tailored to lower termination impedance ranges where P_{rx} peaks. This paper presents comprehensive simulations—finite element method (FEM), distributed circuit modeling—and in-vivo experiments to characterize the body channel as a finite impedance wire, with impedance determined by body dimensions. Contact impedance between the body and receiver, inversely related to contact area, significantly affects P_{rx}, necessitating careful design for devices with small contact areas. Furthermore, the body cross-sectional area influences voltage recovery after the point of load, with smaller cross-sections yielding reduced recovery. A lumped circuit model is developed to encapsulate these findings with circuit techniques to maximize P_{rx}, demonstrating that series resonance in a ground-floated receiver reduces input impedance by over 65x and improves P_{rx} by more than 25x over parallel resonance. We also propose a method to approximate optimal loading impedance for various receiver configurations and analyze the impact of inductor Q factor. We prove that neither series nor parallel resonance can mitigate the transmitter return path capacitance. These insights enable the development of a much higher on-body wireless power transfer method, advancing wearable device technology for applications in healthcare, fitness, and beyond.**

***Index Terms*— Capacitive Human Body Powering (HBP), Wireless Body Area Networks (WBAN), Electro-Quasistatic (EQS), Finite Element Method (FEM), Biophysical Modeling, Circuit Analysis**

I. Introduction

At the onset of the next technology revolution, enabling human-machine symbiosis is a common theme across many research fields, ranging from better artificial intelligence models to more capable wearable devices containing them [1]–[4]. With unique human physiological data collection properties and the need for the human-machine interface, the Internet of Bodies (IoB) [5] is created to provide a low-latency, high bandwidth, and low-energy network on and around the body. However, powering on-body devices remains a problem even with the creation of such a network. Traditionally, these devices are battery-powered and require frequent recharging – sometimes daily or multiple times per day. This not only interrupts continuous usage but also makes the task of recharging increasingly burdensome as the number of devices increases. The charging frequency could be reduced with low-power communication techniques such as human-body communication (HBC) [1]. Still, convenient energy harvesting techniques and wireless power transfer techniques are required to eliminate such needs.

Research has demonstrated the use of capacitive-HBC for wireless power transfer in the mega-hertz region [6]–[9]. Specifically, there are two distinct modes of capacitive HBC that separate around 30MHz, a frequency at which the body transitions from functioning as a highly inefficient antenna to a quarter-wave radiative antenna [10]. In the frequency where the body operates as a highly inefficient antenna, the transmission wavelength significantly exceeds the body length. Previous research has demonstrated that, with high-impedance termination, the surface voltage throughout the whole body is almost equal and can be simplified into an equipotential surface and be further simplified into a node. This frequency range is termed the electro-quasistatic (EQS) range [10]. The benefit of operating in the EQS range for powering is two-fold. First, with less radiation, more signals are contained within the body, increasing the powering efficiency. Second, as the body is not resonating at the operating frequency, there is no need to match the operating frequency to the body length, reducing the operational complexity.

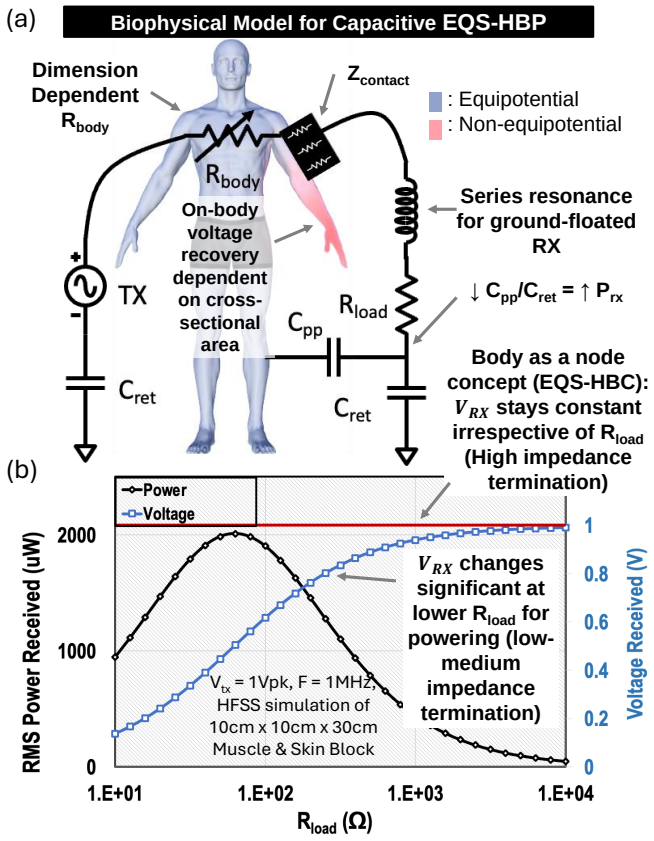

Fig. 1. (a) capacitive EQS-HBP lumped circuit model from the insights into body channel modeling. (b) While capacitive EQS-HBC considers the body as an equipotential surface due to high impedance termination, capacitive EQS-HBP, where power is maximized at lower loading impedance, cannot make this assumption. Therefore, a more detailed analysis of body channel modeling is required. This plot is generated using HFSS with muscle and skin blocks, as shown in Fig 3(b).

Despite a myriad of studies on biophysical modeling for EQS-HBC [10]–[24], there lacks an in-depth equivalent analysis of EQS human body powering (EQS-HBP) to guide future research and development of EQS-HBP applications. Even with the operational similarity between EQS-HBC and EQS-HBP, they are fundamentally optimized for different outcomes. EQS-HBC aims to enhance channel

capacity between the transmitter (TX) and receiver (RX), with high-impedance termination facilitating this goal [10]. In contrast, EQS-HBP focuses on maximizing the P_{rx}, which requires impedance matching; higher termination impedance does not increase power transfer, as illustrated in Fig 1(b). Additionally, there are two modes of EQS-HBP: capacitive and galvanic. In comparison, capacitive EQS-HBP is much better at providing full body coverage. Thus, this paper focuses on exploring channel behaviors at lower impedance range and developing a biophysical model for capacitive EQS-HBP. Using that, a detailed analysis of the circuit theory of the capacitive EQS-HBP is performed to optimize powering performance.

In-depth analysis reveals three key insights in biophysical modeling: (I) In the EQS frequency range, the body behaves as a finite impedance wire, with its impedance being a function of the bulk conductivity and the body dimension. Using that, voltage distribution across the body can be modeled reliably, and lower body impedance (R_{body}) will lead to a higher peak power received (P_{rx}). (II) In capacitive EQS-HBP, when the contact area is not sufficiently large, there exists a contact impedance in series with the RX that further reduces the P_{rx}. P_{rx} is a strong function of contact area, and minimizing that is key to increasing P_{rx}. (III) Recovery of on-body voltage after the point of load depends on the cross-sectional area of the body. The lower the cross-sectional area, the lower the recovery of on-body voltage after the point of load. A lumped circuit model is developed to capture these insights as shown in Fig 1(a).

With these insights, an in-depth analysis of capacitive EQS-HBP circuit theories for higher P_{rx} has revealed a few key findings: (I) Series resonance will significantly increase the P_{rx} when used on both TX and RX. An analysis and comparison between parallel and series resonance for the ground-floated RX provide analytical proof that series resonance can cancel the effect of return path capacitance (C_{ret}[1]) and reduce the RX input impedance (Z_{in}), leading to higher current and, thus, higher P_{rx}. (II) Series resonance, although it increases voltage coupled from the TX to the body, is unable to cancel the effect of C_{ret} for the TX. (III) P_{rx} through series resonance is sensitive to inductor Q factor, and a higher Q factor will lead to higher P_{rx}. (IV) A method to approximate the optimal loading impedance (R_{load}) for RX for maximum P_{rx} is proposed.

The key contributions of this paper are summarized as:

- Biophysical modeling of body channel for EQS-HBP
  - Body as uniformly distributed finite impedance wire (R_{body})
  - Contact impedance ($Z_{contact}$)
  - Recovery of on-body voltage after point of load
- Circuit optimization of capacitive EQS-HBP
  - Series resonance canceling C_{ret} for the RX but not the TX
  - Effect of inductor Q factor on P_{rx}
  - Approximation for the optimal R_{load} for maximizing P_{rx}

The subsequent sections are arranged as Section II provides the background related to EQS-HBP and related work on biophysical modeling. Section III models the body as R_{body}. Section IV adds $Z_{contact}$ to the lumped circuit model. Section V investigates voltage recovery after the point of load. Section VI uses circuit theory to maximize P_{rx}. Section VII validates the analysis in the previous sections with in-vivo experiments. Section VIII summarizes and discusses the key findings, with IX as the conclusion.

[1]Formally expressed as $C_{xG\infty}$, where $C_{G\infty}$ represents the device's self-capacitance and x is the percentage of the fringe field terminating on the human body, reducing the original self-capacitance. For a detailed explanation, see [12], [15]. In this paper, we use C_{ret} for a more intuitive notation.

II. Background and Related Work

Before EQS-HBP, EQS-HBC was first developed as a low-energy and high-bandwidth alternative in the near-body communication space [5], [25]–[27]. HBC is a data communication technique, and it also has two modes of operation: capacitive [10] and galvanic [28]. In comparison, capacitive EQS-HBC provides better full-body coverage, and the same technique could be used to transfer power through the body wirelessly. Typically, a wearable TX and RX are attached to the body through their signal electrode, with their ground electrode left floating. The TX sends an AC signal to the RX through the body tissue. The signal return path is formed through the RX floating ground, the environmental Earth ground, and the TX floating ground [15]. As the return path is completed through parasitic capacitances between the device floating ground to the environmental Earth ground, this method is thus termed capacitive EQS-HBP.

A. Capacitive EQS-HBC as Voltage Mode Communication

The need for a comprehensive channel and circuit analysis of capacitive EQS-HBP stems from the voltage mode communication technique employed in capacitive EQS-HBC. Traditional wireless communication systems use power mode communication, where maximizing the received signal power leads to maximizing the overall system performance, and the signal propagation through the air channel is primarily described by power transmission. In contrast, capacitive EQS-HBC operates at a wavelength larger than the scale of the body. While a time-varying E-field is present, the H-field is not significant, so $\frac{dH}{dt}$ does not substantially impact the E-field. As a result, the system can be primarily approximated as electro-quasi-static. Therefore, capacitive EQS-HBC is referred to as voltage mode communication, and optimizing the system performance requires high impedance termination [10], [12], [15], leaving the channel characteristics of lower to medium impedance termination range unexplored. While high-impedance termination is commonly employed in capacitive EQS-HBC, providing a clear, intuitive explanation will facilitate better understanding, enabling easier comparisons with capacitive EQS-HBP.

The primary motivation for high-impedance termination over impedance matching in capacitive EQS-HBC is to maximize channel

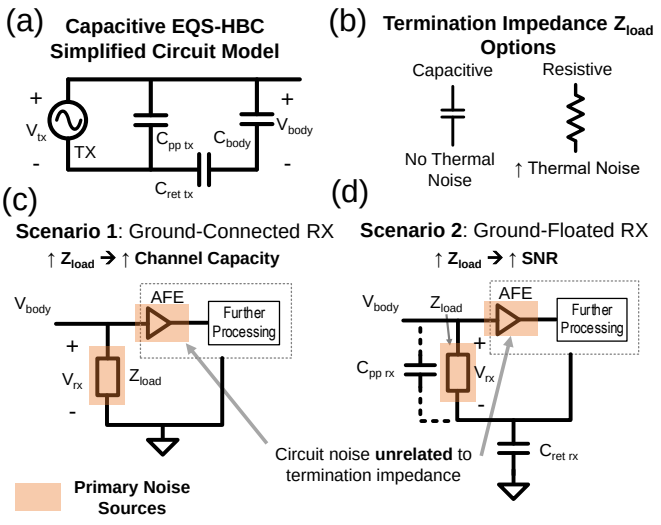

Fig. 2. (a) Simplified circuit model of capacitive EQS-HBC. (b) Termination impedance options. (c) Scenario 1: ground-connected RX. High impedance termination boosts channel capacity. (d) Scenario 2: ground-floated RX. High impedance termination boosts SNR.

capacity. This concept can be illustrated through two distinct scenarios involving signal-to-noise ratio (SNR) and channel bandwidth.

In the first scenario, the RX is a ground-connected device (without C_{ret}), as depicted in Fig 2(c). Here, the primary noise sources include input termination resistance and circuit noise, which can be expressed as $V_N^2 = 4kTR + V_{N_{ckt}}^2$. The received voltage can be approximated as $V_{rx} = \frac{R}{R+Z_{body}} * V_{tx}$. When $R \gg Z_{body}$, $V_{rx} \approx V_{body}$ (Fig 1(b)), and further R increment does not improve V_{rx}; instead, only $4kTR$ noise is increased, degrading SNR. This issue can be mitigated by employing capacitive termination, as only the equivalent series resistance (ESR) of the capacitor will contribute to the noise. Despite the SNR will eventually plateau when $Z_{load} \gg Z_{body}$, increasing the Z_{load} will enhance the body channel bandwidth [10]. According to Shannon's capacity theorem ($Capacity = BW \log_2(1+SNR)$), higher bandwidth leads to increased channel capacity, enabling either higher data rates or reduced energy consumption for a given data rate. Therefore, maximizing the Z_{load} is desirable.

In the second scenario, the RX is a ground-floated device (with C_{ret}), as shown in Fig 2(d). The received voltage can be approximated by $V_{rx} = \frac{Z_{load}}{Z_{load}+Z_{C_{ret}}} * V_{body}$ and V_{body} is constant regardless of Z_{load} due to $Z_{C_{ret}} \gg Z_{body}$, resulting in an SNR expression of $SNR = V_{rx}^2/V_N^2 \propto Z_{load}$ when $Z_{load} \ll Z_{C_{ret}}$. Given that C_{ret} typically falls within the pico-farad range [15], it presents a high AC impedance, exceeding $100\,k\Omega$ at 1MHz, making the $Z_{load} \ll Z_{C_{ret}}$ condition generally applicable. This condition favors increasing Z_{load} as much as possible. In the extreme case where $Z_{load} \to \infty$, $V_{rx} = V_{body} * \frac{C_{ret}}{C_{ret}+C_{pp}}$ [2].

Lastly, with interference, increasing Z_{load} may not necessarily improve the signal-to-interference ratio (SIR). If the interference frequency is close to the signal frequency, altering Z_{load} will have no effect on SIR. However, if the interference frequency is significantly higher (e.g., 2.4GHz), the low-pass filtering properties of the body channel will naturally attenuate it. Conversely, if the interference frequency is significantly lower (e.g., 50-60Hz power line interference), a high-pass filter could be employed to attenuate the interference without changing Z_{load}.

While capacitive EQS-HBC focuses on maximizing channel capacity through high-impedance termination, capacitive EQS-HBP aims to maximize P_{rx}, which necessitates impedance matching. The following sections examine the biophysical model in detail to identify the key elements for achieving impedance matching.

B. Capacitive EQS-HBP Related Work

Maity et al. carry out experiments between 10KHz and 1MHz, modeling the body channel for capacitive EQS-HBC and generating values for the different elements of the circuit model [10]. The body is modeled as a network of resistors and capacitors. The exact values of resistor and capacitor can vary between subjects and environments, but a typical range of values is proposed. However, as the experiments were done with high-impedance termination, the insights do not apply readily to low to medium impedance termination scenarios.

Modak et al. have calculated the peak power transfer for ground-floated TX and RX scenario [6]. However, the circuit model used is a variant of the model proposed by Maity et al. that the body is considered as an equipotential surface with channel loss dominated by parasitic capacitance, leaving impedance matching for maximum P_{rx} unexplored. Furthermore, Modak et al. only focused on the TX circuit optimization, leaving the RX circuit optimization unexplored.

Cho et al. have modeled the body channel for capacitive EQS-HBP as a capacitive dominant circuit with the body channel as C_B and R_B, and explored the ground-floated TX and RX scenario [9]. Similar to Modek et al., the body channel has not been studied across termination impedance, with optimization focusing solely on TX.

Hitherto, research efforts to improve capacitive EQS-HBP have largely relied on models proposed for EQS-HBC [6], [9]. Optimization efforts have been mainly confined to TX instead of exploring the effect of R_{body}, the device parameters, such as contact area size and C_{ret}, and the RX circuit theory to increase P_{rx} [6], [9].

Although this work only focuses on the EQS region, it is possible to transfer power through the body channel above the EQS region [29]–[38]. Li et al. have demonstrated this, and named it body-coupled powering (BCP) [7]. When the wavelength approaches and is smaller than the body dimension, the body starts to become radiative. HBP biophysical modeling for that region would need to include the radiative loss as part of the modeling, which can be omitted in the EQS region. Furthermore, as the body becomes radiative, the on-body voltage distribution starts to deviate from that of the EQS region and may share more similarities with a quarter-wavelength antenna.

Within the EQS region, past research has modeled body channel using distributed analysis [13] and lumped analysis [9], [39]. In distributed analysis, the body is broken into many smaller units, and each unit is characterized and represented through passive components such as resistors and capacitors. In comparison, in lumped analysis, the body is treated as a homogeneous subject and represented by only a few resistors and capacitors. Although lumped analysis lacks the level of detail and accuracy of distributed analysis, it does capture the essential phenomenon of the body channel in the region of interest and facilitates intuitive interpretation of results. Furthermore, lumped analysis aids in the practical design of body-based communication and powering systems by highlighting the most important components, similar to the first few basis vectors in the principal component analysis. For example, Maity et al. and Datta et al. have shown the biophysical model for capacitive EQS-HBC can

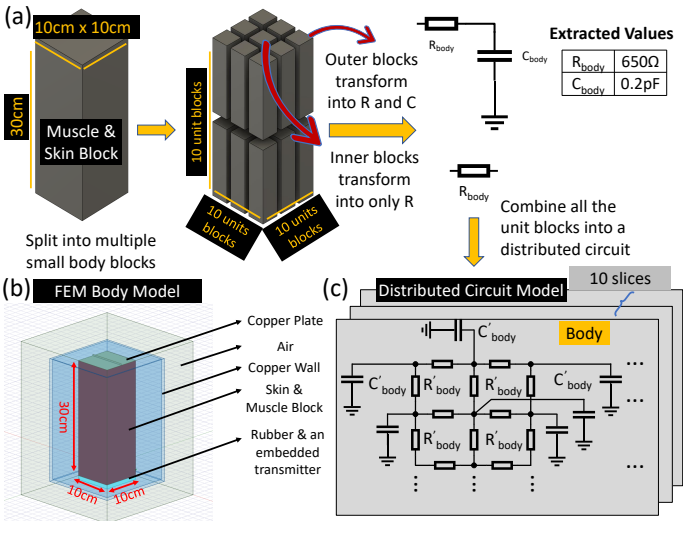

Fig. 3. (a) illustrates generating the distributed RC circuit from a 30cm x 10cm x 10cm skin & muscle block by dividing it into smaller unit blocks (10 per dimension) and combining them into the circuit in (c). The outer unit blocks are represented as $\boldsymbol{R'_{body}}$ and $\boldsymbol{C'_{body}}$. The inner unit blocks are represented as $\boldsymbol{R'_{body}}$. (b) shows the HFSS model of it.

[2] As shown in [12], the total parasitic capacitance between the device ground electrode and the human body, denoted as C_{GB}, comprises the parallel plate capacitance between the signal and ground electrodes and the fringe capacitance from the device ground plate to the body. For intuitive notation, this paper refers to it as C_{pp}.

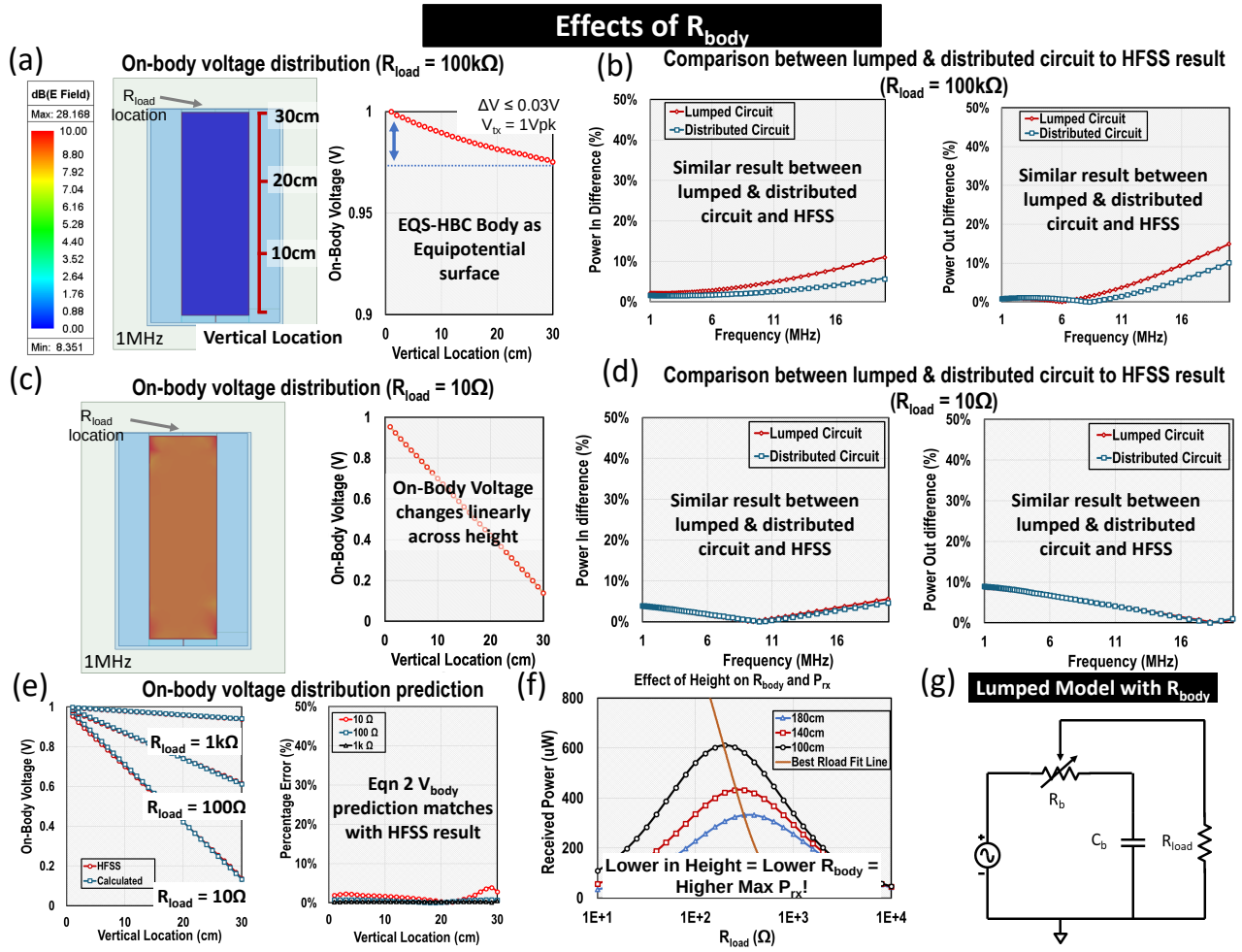

Fig. 4. (a) Simulation results from HFSS, distributed circuit, and lumped circuit models for $\mathbf{100k\Omega}$ load. (c) Simulation results for $\mathbf{10\Omega}$ load. (b) and (d) Percentage error between lumped & distributed circuit to HFSS results, for $\boldsymbol{R_{load} = 100k\Omega}$ and $\boldsymbol{R_{load} = 10\Omega}$. (e) Comparison of on-body voltage predictions across various on-body vertical locations and $\boldsymbol{R_{load}}$, with percentage errors under 5%. (f) Effect of height on $\boldsymbol{R_{body}}$ and $\boldsymbol{P_{rx}}$ for a constant cross-sectional area; as height decreases, peak $\boldsymbol{P_{rx}}$ increases. (g) Lumped circuit model with $\boldsymbol{R_{body}}$.

be reduced to only R_{body} and C_{body}, and it is even possible to omit R_{body} if high impedance termination is used [10], [12].

Thus, this paper adopts the approach of investigating the physical phenomenon of the biological body channel for capacitive EQS-HBP through distributed analysis to develop an intuitive lumped model that captures the biophysical behaviors.

III. Body as Uniformly Distributed Finite Impedance Wire (R_{body})

Maximizing P_{rx} requires impedance matching, necessitating an investigation into modeling the body in the lower impedance range.

A. Modeling Human Body for Powering

Modeling the body channel in simulation is crucial to discern the second-order effects from the first-order effects that often plague physical experiments, facilitating a clearer understanding of the primary influences on P_{rx}. Thus, the simplified body is analyzed through finite element method (FEM) based simulation using Ansys High-Frequency Structure Simulator (HFSS) and distributed resistor-capacitor (RC) circuit. as shown in Fig 3.

In capacitive EQS-HBP, the TX couples an AC signal onto the body, and the RX is placed on the body to drive a load using the coupled AC signal. The TX and RX can have their ground floating or connected to the environmental ground. The main difference between ground-floated and ground-connected is the presence and absence of C_{ret}. The C_{ret} introduces a high series-connected AC impedance and thus reduces the amount of current into and out of the system. This behavior could be captured by analyzing the body from low to high R_{load}. Thus, in the HFSS simulation, both the TX and RX are ground-connected, with R_{load} sweeping across the resistance range. Furthermore, to simplify the analysis and capture major first-order effects, the simplified body model comprises only muscle and skin.

In the distributed RC circuit, the body is broken into inter-connected unit blocks, as shown in Fig 3(c). The effect of skin impedance is negligible when analyzing R_{body} as $Z_{skin} \ll R_{body}$ ($C_{skin} > 500pF$ for $4cm^2$ [10])). Thus, each unit block comprises a unit resistor, representing muscle unit impedance, and a unit capacitor, representing unit C_{body}. Depending on if other unit blocks fully enclose the unit block, the unit C_{body} may be absent.

B. Body impedance

As established in earlier sections, E-field predominate in the EQS range. Thus, R_{body} should be dependent on the body dimension and the bulk material (muscle) conductivity and can be approximated using Eqn 1, where H_b is the height, A_b is the toro cross-sectional area, and f is the operating frequency:

$$R_{body} \approx F(v, \sigma(f)) = H_b * \frac{1}{A_b} * \frac{1}{\sigma(f)} \quad (1)$$

HFSS and distributed circuit simulations are conducted across two ends of the impedance and EQS frequency range to verify this

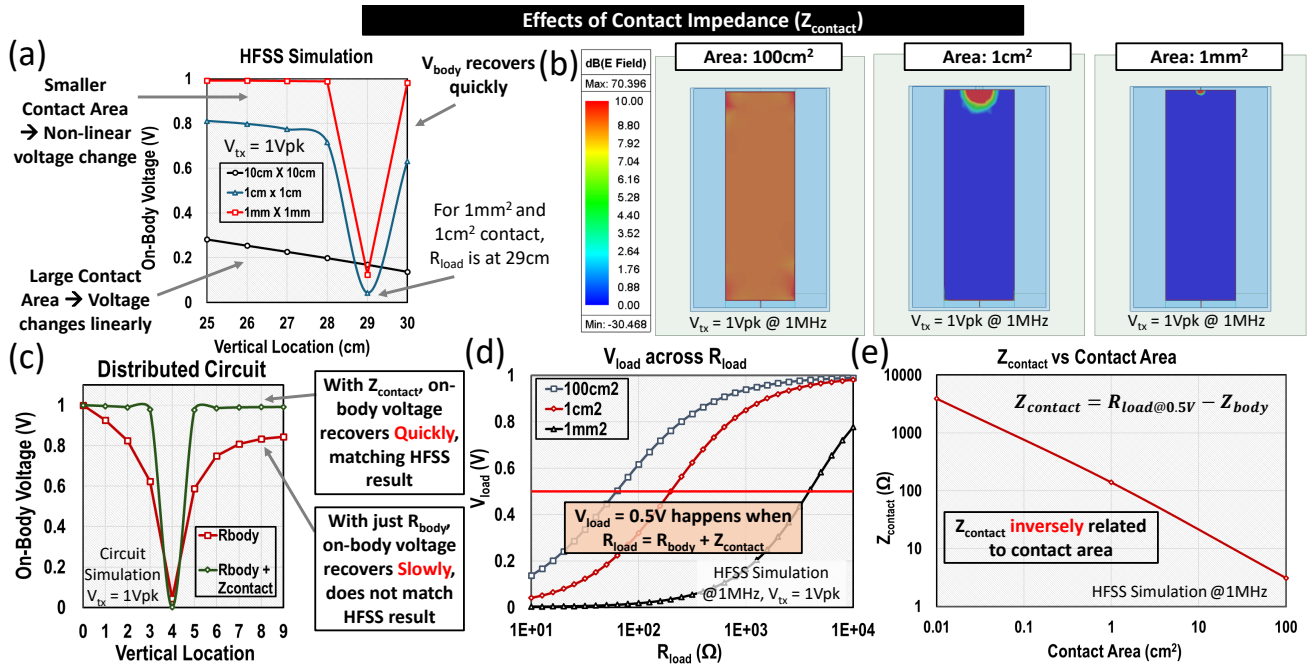

Fig. 5. (a) Variation of on-body voltage across vertical locations for $\boldsymbol{R_{load} = 10\Omega}$ with three different contact areas: $\mathbf{100cm^2}$, $\mathbf{1cm^2}$, and $\mathbf{1mm^2}$. (b) HFSS Field plot of (a), with $\boldsymbol{V_{load}}$ shown in (d). (c) Inclusion of $\boldsymbol{Z_{contact}}$ matches distributed circuit to HFSS results. (d) $\boldsymbol{V_{load}}$ variation against $\boldsymbol{R_{load}}$ across the three contact sizes. (e) Change in $\boldsymbol{Z_{contact}}$ with respect to contact area at 1MHz.

equation. Furthermore, using the same R_{body} and C_{body}, calculations using the lumped circuit model are also compared. The simulation aims to verify (1) Eqn 1 and (2) if a lumped circuit can be used to describe capacitive EQS-HBP.

Experiment results in Fig 4 (a)-(d) show that all three methods yield similar trends and values for input and output power. The values align with each other better at lower frequency as compared to higher frequency but overall, the differences $\leq 10\%$. Furthermore, at higher R_{load}, the voltage variation across the body is minimal, showing the body channel as equipotential. At lower R_{load}, the on-body voltage changes linearly across the body, suggesting a uniform distribution of R_{body} across height, enabling location-based on-body voltage prediction using Eqn 2, where loc refers to the distance from the point of interest to the TX location.

$$V(loc) = V_{tx} - R_b(loc) \times I(R_{load}, R_b) \tag{2}$$

As shown in Fig 4(e), the calculated result using Eqn 2 aligns closely with the HFSS simulation result across multiple R_{load}. The percentage error in all cases is less than 5%, verifying that R_{body} is uniformly distributed across height.

C. Key Takeaway

In the EQS range, the body can be modeled as a uniformly distributed resistor (R_{body}) (Fig 4(g)), with R_{body} calculated using Eqn 1. When $R_{load} \gg R_{body}$, the on-body voltage shows minimal variation, allowing the body channel to be approximated as equipotential, consistent with the general model of capacitive EQS-HBC [10], [12]. When R_{load} is comparable to R_{body}, the on-body voltage varies linearly (Fig 4(e)), and can be predicted using Eqn 2. Fig 4(f) demonstrates the effect of R_{body} on P_{rx}; a shorter person with similar body diameter has a lower R_{body}, resulting in higher peak P_{rx}. This section also validates that the lumped circuit model still describes circuit behavior within the EQS region.

IV. Contact Impedance ($Z_{contact}$)

During simulation, the contact area also critically impacts P_{rx}. The simulation result (Fig 5(a)), shows that at a larger contact area, the on-body voltage change is linear, and the body behaves as a uniformly distributed resistor. However, at a lower contact area, the on-body voltage variation across height changes non-linearly, and when the contact area is very small, the body approaches equipotential except at the point of load. Modeling this behavior is crucial as the typical wearable contact area is in the order of $1cm^2$, and the typical brain implantable contact area is in the order of $1mm^2$.

A. Simulation

To investigate this behavior, HFSS simulations are conducted (Fig 5 (a) and (b)). The bottom of the body block connects to the ground-connected TX that outputs a 1MHz 1Vpk signal. The top of the body block connects to a ground-connected R_{load}. The R_{load} connects to the body through a perfect conductor of varying contact area: 10cm x 10cm, 1cm x 1cm, and 1mm x 1mm. The voltage across the R_{load} is measured as V_{load} with a resistance sweep across contact areas.

B. Result

For the lumped circuit model shown in Fig 4(g), if the pole frequency of the RC circuit (R_{body} and C_{body}) is much higher than the operating frequency, minimal current flows through C_{body}. This allows the circuit to be simplified to a resistance-dominated model, with node voltages calculated using the resistor ladder formula. Consequently, V_{load} can be approximated as $V_{tx}/2$ when $R_{load} = R_{body}$. As shown in Fig 5(e), achieving $V_{tx}/2$ requires that the R_{load} increase by one magnitude order when the contact area decreases by one magnitude order. Since body dimensions and operating frequency are constant across these simulations, R_{body} remains constant. Therefore, an additional impedance, named contact impedance ($Z_{contact}$), exists at the load point, with its value dependent on the contact area size. The updated circuit diagram, incorporating $Z_{contact}$, is shown in Fig 6(a).

The effect of $Z_{contact}$ is further demonstrated in Fig 5(c). The same simulation is conducted in both HFSS and distributed circuit models, with and without $Z_{contact}$. With only R_{body}, the distributed circuit simulation does not align with the HFSS simulation results in

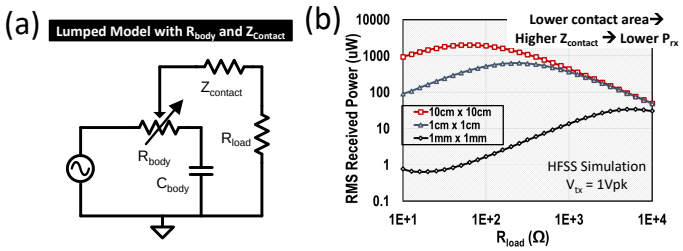

Fig. 6. (a) Final lumped circuit model for capacitive EQS-HBP, where the body channel is represented as a uniformly distributed finite-impedance wire with an additional contact impedance, $\boldsymbol{Z_{contact}}$. (b) Impact of contact impedance on $\boldsymbol{P_{rx}}$: a smaller contact area results in higher contact impedance, reducing the $\boldsymbol{P_{rx}}$.

terms of on-body voltage variation trends. However, with $Z_{contact}$ added, the distributed circuit simulation results align closely with those of HFSS. By incorporating $Z_{contact}$, the distributed circuit model effectively represents the voltage changes observed in HFSS.

C. Key Takeaway

The presence of an area-dependent impedance at the contact point is the second essential component in the lumped circuit model, completing the first-order biophysical model of the body for capacitive EQS-HBP. $Z_{contact}$, shown in Fig 5(e), exhibits an inverse relationship with contact area. At around $1cm^2$ or smaller, $Z_{contact} \geq R_{body}$. The impact of $Z_{contact}$ is illustrated in Fig 6(b), where a larger contact area leads to a higher peak P_{rx}. Intuitively, when $R_{load} \ll R_{body}$, the small size of the contact area restricts the free flow of electrons through the load to the ground, causing a build-up of electrons around the contact point, leading to a rapid drop in on-body voltage (thus $Z_{contact}$) near the contact location (Fig 5(b)). The origin of $Z_{contact}$ requires further investigation and may be influenced by multiple factors. One hypothesis is that $Z_{contact}$ is linked to R_{body} through dimensions, with lower contact areas yielding higher effective R_{body} at the contact point compared to larger areas, as indicated by the inverse relationship in Eqn 1. Another hypothesis is that $Z_{contact}$ is related to skin impedance, which is typically neglected in R_{body} calculations. Further research into these hypotheses is necessary to fully understand the origin of $Z_{contact}$ and its frequency dependence. For practical applications, on-body devices with larger contact areas will yield higher available power, and typical wearables should aim for a contact area of at least 1cm^2.

V. Recovery of On-Body Voltage

Sections III and IV simplify the body into lumped circuit elements to facilitate intuitive analysis. However, modeling the body as $R_{body} + Z_{contact}$ still leaves one open question: how does body potential vary at different points when a small R_{load} is attached? Two trends observed from earlier in-vivo experiments and FEM-based torso and limb simulations offer insight. When a small R_{load} is attached to the torso, on-body voltage generally recovers to levels similar to those before the load point, as shown in Fig 5(a) and (c). However, in similar simulations on a limb, on-body voltage does not fully recover to before the load point levels, as shown in Fig 7(f). This suggests that the torso and limbs behave differently under load, and this section presents FEM simulations to demonstrate that this difference arises from variations in cross-sectional area.

A. Simulation

The FEM simulations are shown in Fig 7(a) and (b). As in Sections III and IV, the bottom of the body block connects to a ground-connected TX, outputting a 1MHz, 1Vpk signal, and a 10Ω load

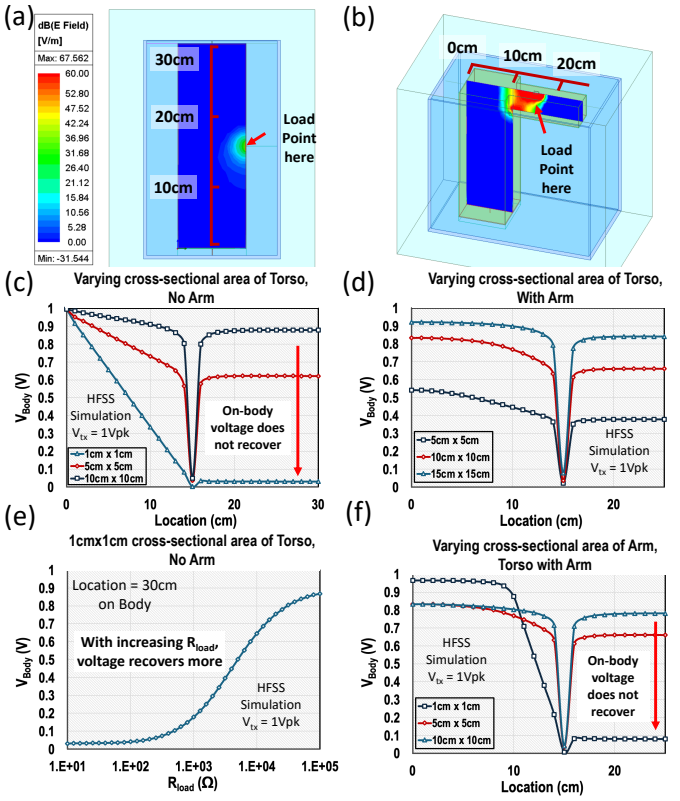

Fig. 7. (a) HFSS model with torso and without limb. Three different torso cross-sectional areas were simulated, and the results are shown in (c). (e) shows $\boldsymbol{V_{body}}$ at height = 30cm along the torso with cross-sectional area of $\boldsymbol{1cm^2}$, evaluated against changes in $\boldsymbol{R_{load}}$. (b) HFSS model with both torso and limb. Three different torso cross-sectional areas were simulated, as shown in (d). (f) presents simulation results for the model in (b), varying the cross-sectional area of the limb (arm) while keeping the torso cross-sectional area constant.

with a 1cm x 1cm contact area attaches to the body. Three primary simulations were conducted. (I) The model consists of only the torso with three different cross-sectional areas, with the load point located at the midpoint along the torso length to observe voltage recovery beyond the load point. (II) The model includes one limb and the torso, with the load applied at the limb. Here, the torso has three different cross-sectional areas to examine how the torso cross-sectional area affects voltage recovery on the limb. (III) The model also includes a limb and the torso, with the load attached to the limb. This time, the limb has three different cross-sectional areas to assess voltage recovery within the limb. Fig 7 (a) depicts the setup for simulation (I), while Fig 7 (b) shows the setups for simulations (II) and (III).

B. Result

In Fig 7(c), we observe that as the torso cross-sectional area decreases, the ability of the torso to recover on-body voltage after the small R_{load} load point diminishes. With a torso cross-sectional area of 100cm^2, the on-body voltage nearly returns to the transmitted voltage (V_{tx}), and the body behaves as an equipotential surface, except at the load point. Conversely, with a torso cross-sectional area of 1cm^2, the on-body voltage does not recover after the small R_{load}, causing the body to behave as if shorted to ground at the load point. This behavior is similarly observed in Fig 7(f) in the presence of a limb. When the limb cross-sectional area is large ($> 100\text{cm}^2$), the on-body voltage recovers after the small R_{load}. However, when the limb cross-sectional area is small, the on-body voltage fails to recover after the load point.

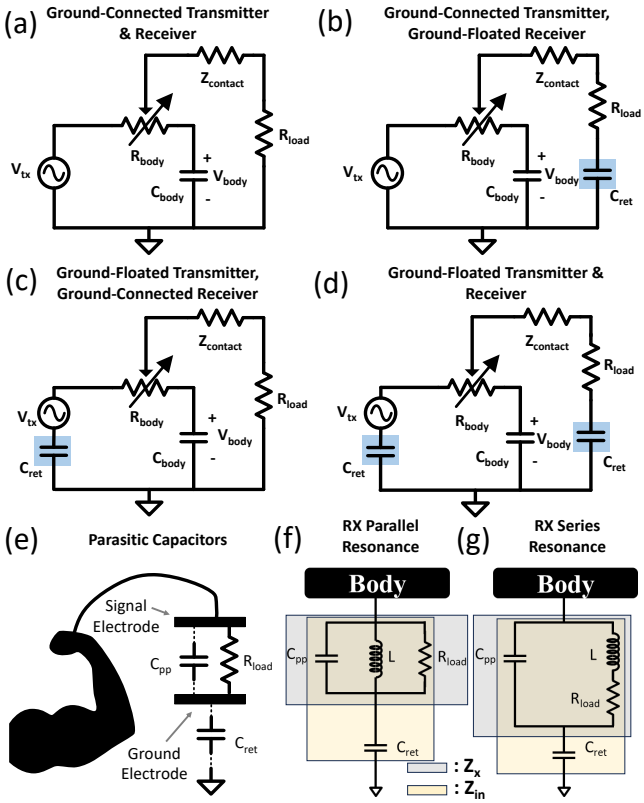

Fig. 8. (a), (b), (c), and (d) show the four configurations of capacitive EQS-HBP. (e) highlights the primary parasitic capacitors, labeled as $\boldsymbol{C_{pp}}$ and $\boldsymbol{C_{ret}}$. (f) depicts the circuit configuration for parallel resonance, while (g) shows the configuration for series resonance.

Fig 7(d) serves as a reference. With one limb and a fixed cross-sectional area, varying the torso cross-sectional area does not change the on-body voltage recovery on the limb; it only changes the general on-body voltage, as the general R_{body} changes with the torso cross-sectional area. Additionally, the degree of on-body recovery depends on the R_{load} as well. As shown in Fig 7(e), at the same distance from the point of load, if the R_{load} is higher, the on-body voltage recovers more.

C. Key Takeaway

When R_{load} is attached to the body, the degree of on-body voltage recovery after the load point depends on both the cross-sectional area of the body region and the R_{load}. As either the cross-sectional area or the R_{load} decreases, the on-body voltage recovery after the load point is reduced. Since capacitive EQS-HBP aims to maximize P_{rx}, R_{load} should be impedance matched to $R_{body}+Z_{contact}$. Given that typical human limb cross-sectional areas are in the order of tens of cm^2, careful placement of on-body RXs is essential to minimize the negative impact of reduced on-body voltage recovery. For instance, if multiple power RXs are placed on the body, higher total power can be achieved by avoiding placement exclusively on the limbs, as limbs generally have a smaller cross-sectional area than the torso. Additionally, if two power RXs are placed on the same limb, the RX closer to the torso should be designed to avoid significantly reducing the power available to the second RX by balancing its power draw.

VI. Circuit Optimization for Capacitive EQS-HBP

Optimizing the P_{rx} in capacitive EQS-HBP is multi-faceted; it includes channel modeling, device optimization, and even environment modeling and optimization. After modeling the body with $R_{body} + Z_{contact}$, this section investigates circuit optimization to boost P_{rx}. Capacitive EQS-HBP can occur in four distinct configurations based on the ground-connectedness, as illustrated in Fig 8 (a)-(d). This ground-connectedness is sometimes also referred to as machine or wearable, in which ground-connected devices are considered as a machine as it is plugged into the electrical outlet and connected to the environmental ground, and ground-floated devices are considered as wearables where the ground electrode is left floating.

A. Previous Work

When the TX or RX is ground-floated, the device ground is not physically connected to the environmental ground but weakly coupled to it through C_{ret}, which Nath et al. have investigated [15]. In addition to C_{ret}, another parasitic capacitance named C_{pp} also critically affects the performance as it shunts current away from R_{load}. C_{pp} is the parasitic capacitance between the signal and ground electrode and can be boosted from an effect known as body shadowing, which Datta et al. have investigated [12]. To intuitively visualize C_{ret} and C_{pp}, they are shown in Fig 8(e).

As C_{ret} limits the effective device current into and out of the body, it attenuates the power transmitted and received. To counteract the effect of it, inductive elements could be introduced to produce opposing reactive impacts. Modak et al. have investigated TX resonance [6]. They proposed two kinds of resonance: parallel and series. For parallel resonance, an inductor is added between the TX ground and signal electrode. At resonance, this inductor resonates with C_{pp} to reduce the shunt current through C_{pp} and increase the powering efficiency. For series resonance, an inductor is added between the TX signal electrode and the body. At resonance, this inductor resonates with C_{pp} and C_{ret} to boost on-body voltage at the expense of more shunt current. However, the exact cancellation of C_{ret} remains unexplored.

Despite a lack of prior examples of RX optimization for capacitive EQS-HBP, RX parallel resonance (Fig 8(f)) has been demonstrated to boost the P_{rx} beyond the EQS frequency range [7]. This technique could also be used for capacitive EQS-HBP but has yet to be thoroughly investigated. Furthermore, similar to TX, RX series resonance (Fig 8(g)) is also possible. Hitherto, an in-depth analysis of the optimal resonance technique for capacitive EQS-HBP remains lacking and the following subsection aims to bridge this gap. In addition, since resonance is employed, the following section will also investigate the effect of the inductor Q factor on P_{rx}.

Lastly, since the resonance occurs between the inserted inductor and the TX and RX parasitic capacitance, rather than involving $R_{body} + Z_{contact}$, the circuit analysis will first focus on the TX and RX circuits individually for a simpler analysis. The impact of $R_{body} + Z_{contact}$ will be assessed after.

B. Cancelling the receiver C_{ret} for higher P_{rx}

Circuit simulations with identical parasitic components have shown that series resonance achieves higher P_{rx} compared to parallel resonance or no resonance, as seen in Fig 9(c). To understand the circuit theory behind this, it is essential to consider what the inductor is resonating with. In parallel resonance, the inductor forms a clear LC tank with C_{pp}, and at resonance, the shunt current that would normally flow through C_{pp} in the absence of resonance instead flows through R_{load}, thereby boosting P_{rx}. In series resonance, the LC tank is formed by the inductor along with a combination of C_{pp} and C_{ret}. At resonance, a portion of the C_{ret} is canceled, significantly increasing the input current and enhancing the P_{rx}.

This could be intuitively illustrated with RX Z_{in} circuit equations:

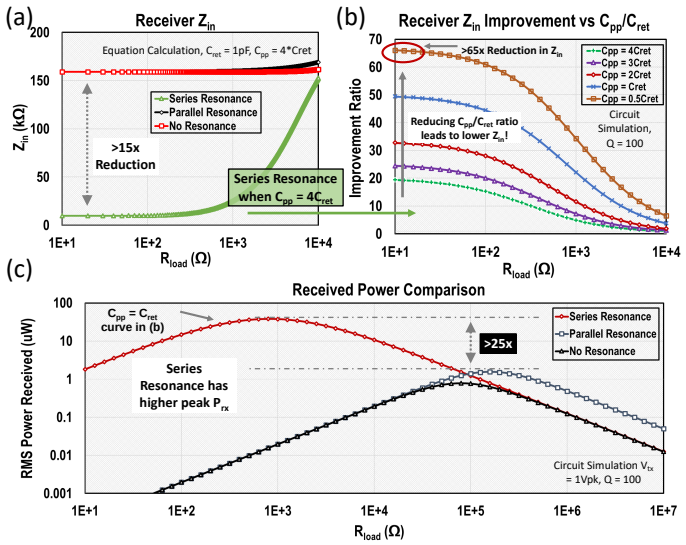

Fig. 9. (a) $\boldsymbol{Z_{in}}$ for series, parallel, and no resonance configurations, all with the same RX parasitic capacitances ($\boldsymbol{C_{pp}}$ = 4pF and $\boldsymbol{C_{ret}}$ = 1pF). (b) Improvement in $\boldsymbol{Z_{in}}$ ($\boldsymbol{Z_{in}}$ parallel resonance/$\boldsymbol{Z_{in}}$ series resonance) across typical $\boldsymbol{C_{pp}/C_{ret}}$ ratios. (c) $\boldsymbol{P_{rx}}$ versus $\boldsymbol{R_{load}}$ for series, parallel, and no resonance configurations under the same conditions as in (a).

$$Z_{in} = Z_{C_{ret}} + Z_X = -\frac{j}{\omega C_{ret}} + Z_X \tag{3}$$

In Eqn 3, Z_X represents the equivalent impedance of the remaining circuit components that are in series to C_{ret}. As $Z_{C_{ret}} = \frac{1}{j\omega C_{ret}}$, it has a negative reactive component and as C_{ret} is small, the absolute magnitude of $Z_{C_{ret}}$ is large. If a positive reactive component could be introduced to the Z_X term to cancel out part of the negative reactive component from the $Z_{C_{ret}}$ term, overall Z_{in} could be reduced.

For parallel resonance, its Z_X is:

$$Z_{X_{parallel}} = R_{load}//Z_L//Z_{C_{pp}} = \frac{LR_{load}}{jR_{load}\omega(LC_{pp} - \frac{1}{\omega^2}) + L} \tag{4}$$

$$\text{At resonance } (\omega = \frac{1}{\sqrt{LC_{pp}}}) : Im(Z_{X_{parallel}}) = 0 \tag{5}$$

The above equation would not have positive reactive components at resonance, corresponding to the major limitation of parallel resonance: it does not cancel C_{ret}. Therefore, the lowest Z_{in} for parallel resonance remains at $Z_{C_{ret}}$.

For series resonance, its Z_X is:

$$Z_{X_{series}} = Z_{C_{pp}}//(Z_L + R_{load}) = \frac{R_{load} + L\omega j}{1 - \omega^2 C_{pp}L + R_{load}C_{pp}\omega j} \tag{6}$$

$$\text{At resonance } (\omega = \frac{1}{\sqrt{L(C_{ret} + C_{pp})}}) : Im(Z_{X_{series}}) > 0 \tag{7}$$

At resonance, the above equation would have positive reactive components due to the $L\omega j$ term in the numerator. This could be easily verified by substituting the variables with actual circuit values. Consequently, part of the C_{ret} gets canceled by series resonance, and Z_{in} could thus be lower than $Z_{C_{ret}}$. The Z_{in} improvement is dependent on R_{load} as it restricts the inductor resonance current. When R_{load} is significantly large, it will stop series resonance and transform the circuit back to no resonance, as shown in Fig 9 (b) and (c). The Z_{in} for series resonance could be derived as shown below:

$$Z_{in} = \sqrt{\frac{k_4 + k_5 R_{load}^2}{k_2 R_{load}^2 + k_3}} \tag{8}$$

$$k_2 = (\omega^2 C_{pp} C_{ret})^2 \tag{9}$$

$$k_3 = (\omega C_{ret} - \omega^3 C_{pp} C_{ret} L)^2 \tag{10}$$

$$k_4 = \left(1 - \omega^2 L(C_{\text{ret}} + C_{\text{pp}})\right)^2 \tag{11}$$

$$k_5 = ((C_{\text{ret}} + C_{\text{pp}})\omega)^2 \tag{12}$$

Fig 9(a) compares Z_{in} across different resonance techniques. The parallel resonance Z_{in} closely resembles that of no resonance at low to moderate R_{load}. As R_{load} is parallel to C_{pp}, the effect of C_{pp} is negligible if $Z_{C_{pp}} \gg R_{load}$. Thus, $Z_{in} \approx Z_{C_{ret}}$ when $R_{load} \ll Z_{C_{ret}}$. With parallel resonance, the LC tank behaves as an open circuit, making the simplified circuit resemble that of no resonance. In contrast, the series resonance Z_{in} is significantly lower. Depending on the ratio between C_{pp} and C_{ret}, it can reach values as low as $2k\Omega$ or lower, which represents a reduction of over 65x compared to the Z_{in} of parallel resonance and no resonance, as shown in Fig 9(b). This substantial reduction in Z_{in} greatly increases the current into RX, enabling higher peak P_{rx}, as also observed in Fig 9(c). Series resonance achieves a higher peak power than parallel resonance, with the optimal R_{load} for maximum P_{rx} occurring at a lower R_{load}.

Additionally, for device form factor optimization, the ratio between C_{pp} and C_{ret} is a crucial parameter. As shown in Fig 9(b), Z_{in} is a strong function of C_{pp}/C_{ret}. If $C_{pp} \leq C_{ret}$, series resonance will be more effective at reducing Z_{in} and boosting P_{rx}.

Lastly, because RX series resonance significantly reduces Z_{in}, with an optimized C_{pp} to C_{ret} ratio, Z_{in} can approach R_{load}. As shown in section III and IV, the body can no longer be considered as equipotential when $Z_{in\ rx}$ is comparator to $R_{body} + Z_{contact}$. This suggests that $R_{body} + Z_{contact}$ should be included in circuit simulation to improve simulation accuracy.

In conclusion, when the RX is ground-floated, a series-connected inductor significantly enhances the P_{rx} by partially canceling $Z_{C_{ret}}$, thereby reducing the RX Z_{in}. For a ground-connected RX, if $Z_{contact}$ is minimized by increasing the contact area, there is little difference between parallel and no resonance, as $Z_{C_{pp}} \gg R_{load}$.

C. The inability for the transmitter to cancel C_{ret}

As Modak et al. have demonstrated, the TX series resonance would increase the power transmitted into the body [6]. This could be observed from Fig 10(b). As the inductor is in resonance with a combination of C_{pp} branch and C_{body} & C_{ret} branch, the impedance seen from the TX source (Z_{in} shown in Fig 10(b)) into the circuit is reduced, and the current flowing out of the TX source increases. With the increase in current flowing through both branches, the voltage across the two branches increases, and it is shown that $V_{C_{pp}} = Q * V_{tx}$ [6]. As $R_{body} \ll Z_{C_{ret}}$, the voltage across the body could be approximated as (shown in Fig 10(b)),

$$V_{body} = Q * V_{tx} * \frac{C_{ret}}{C_{ret} + C_{body}} \tag{13}$$

Furthermore, another inductor could be added in parallel to C_{pp} to reduce the shunt current through it at resonance to achieve higher efficiency, and the series-connected inductor would need to increase inductance in order to maintain the same resonant frequency.

Despite the increase in V_{body} due to resonance, series or a combination of series and parallel resonance will not be able to cancel the effect of C_{ret} for TX. As C_{ret} is in series with C_{body}, the voltage across C_{body} (V_{body}) experiences a capacitive division that causes V_{body} to be nearly 40dB lower than the resonant voltage QV_{tx}, which is the same as $V_{C_{pp}}$. For reference, C_{body} exists in the high 10s of pico-farads (e.g., around 100pF), and C_{ret} exists in the lower pico-farads (e.g., around 1pF). In order to effectively boost

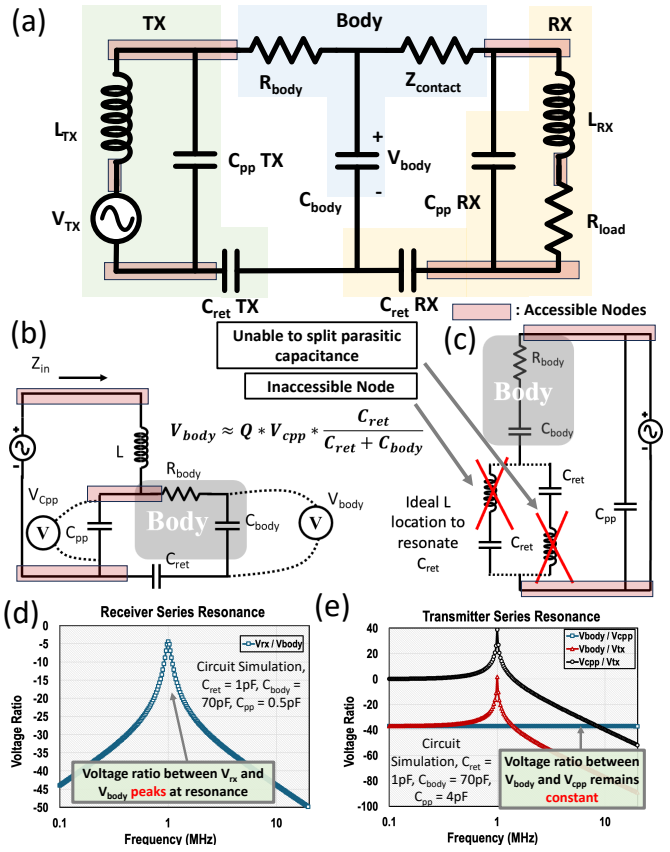

Fig. 10. (a) Series resonance configuration for both TX and RX. (b) Alternative representation of the TX series resonance circuit, emphasizing resonance and the invariance of the $\boldsymbol{V_{body}/V_{C_{pp}}}$ ratio across frequencies. (c) Optimal placement of an inductor to cancel the effect of $\boldsymbol{C_{ret}}$ through resonance. (d) Ratio $\boldsymbol{V_{rx}/V_{body}}$ for a ground-floated RX with series resonance. (e) Three voltage ratios for a ground-floated TX: $\boldsymbol{V_{body}/V_{C_{pp}}}$, $\boldsymbol{V_{body}/V_{tx}}$, and $\boldsymbol{V_{C_{pp}}/V_{tx}}$.

TX ability to couple voltage onto the body, it would be ideal to use resonance to cancel C_{ret} into a short-circuit to remove this capacitive division effect. Resonating out C_{ret} requires placing inductors in series with it, and two configurations of that are shown in Fig 10(c). However, both configurations are not possible as C_{body}, C_{ret} and C_{pp} are parasitic capacitance formed by parasitic coupling between electrodes, environmental ground, and the body surface. This means that it is impossible to insert an inductor in between C_{body} and C_{ret} and also impossible to split C_{ret} and C_{pp} connection by an inductor. Thus, series resonance for the TX is unable to cancel the effect of C_{ret}, unlike that for the RX.

Circuit simulation has been performed to elucidate this concept further. For RX, the goal is to maximize voltage across R_{load} (V_{rx}) given the same V_{body}. For TX, the goal is to maximize V_{body} given the same V_{tx}. In Fig 10(d) which shows RX series resonance, V_{rx}/V_{body} peaks at the resonant frequency, showing the effect of canceling C_{ret} as more on-body voltage gets received across R_{load}. In Fig 10(e) which shows TX series resonance, the voltage ratio between V_{body}/V_{tx} does improve at the resonant point. However, the voltage ratio of $V_{body}/V_{C_{pp}}$ remains constant across frequency, showing the lack of C_{ret} cancellation for the TX. In combination, the TX is coupling voltage onto the body where series resonance does boost current into the body but cannot cancel the capacitive division between C_{ret} and C_{body}, and the RX is receiving voltage from the body to drive R_{load} where series resonance can cancel part of the C_{ret} to significantly reduce the RX Z_{in} and boost the received

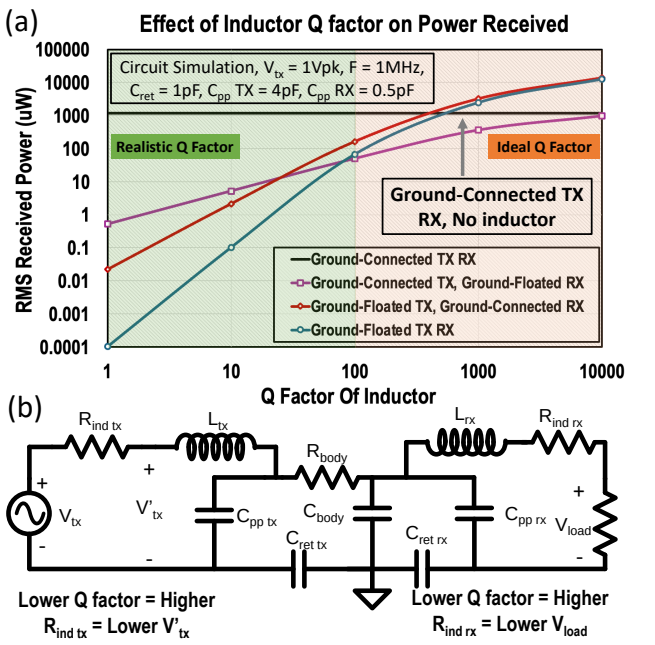

Fig. 11. (a) shows the effect of the inductor Q factor on the $\boldsymbol{P_{rx}}$. This is a circuit simulation across four configurations of capacitive EQS-HBP where an inductor is used and $\boldsymbol{C_{body} = 70pF}$, $\boldsymbol{C_{ret} = 1pF}$, $\boldsymbol{C_{pp_{tx}} = 4pF}$, $\boldsymbol{C_{pp_{rx}} = 1pF}$. (b) shows the circuit diagram with the inductor Q factor modeled as $\boldsymbol{R_{ind}}$ for both TX and RX.

voltage. A combination of the series resonance from the TX and RX side is shown in Fig 10(a). Practically, due to the limited inductor Q factor, series resonance for the TX is unlikely to overcome the near 40dB voltage reduction from the capacitive division, and V_{body} is unlikely to exceed V_{tx}.

D. Effect of Q factor

As the previous subsection introduces the use of an inductive element to achieve higher P_{rx}, the effect of the inductor quality factor on the P_{rx} is investigated in this subsection. Fig 11(a) shows that across the capacitive EQS-HBP where an inductor is used, having a higher quality factor increases the P_{rx} tremendously.

When inductive resonance is used on the TX side, the quality factor could be modeled as a series connected R_{ind} to the inductor, as shown in Fig 11(b). With a high-quality inductor, this R_{ind} is small, and the voltage drop across R_{ind} is low, with the LC circuit having the majority of the V_{tx}. However, with a low-quality inductor, this R_{ind} is large, and the voltage drop across it is high, with the LC circuit having only a fraction of the V_{tx}. Furthermore, when the quality factor is high, according to Eqn 13, V_{body} could be higher than V_{tx}, causing the two ground-floated TX configurations to have a higher P_{rx} than ground-connected TX and RX received cases at high Q factor regions.

When inductive cancellation is used on the RX side, the inductor Q factor determines the amount of R_{ind} series connected with the R_{load}, as shown in Fig 11(c). If the Q factor is high, R_{ind} is kept low with less P_{rx} dissipated by it. As RX inductive cancellation does not boost V_{body}, the highest achievable P_{rx} is similar to that of the ground-connected TX and RX case, with an ideal inductor.

E. Optimal R_{load} for maximizing P_{rx}

With the biophysical circuit model and series resonance technique established in previous sections, this subsection investigates the optimal R_{load} for maximizing P_{rx} across different configurations

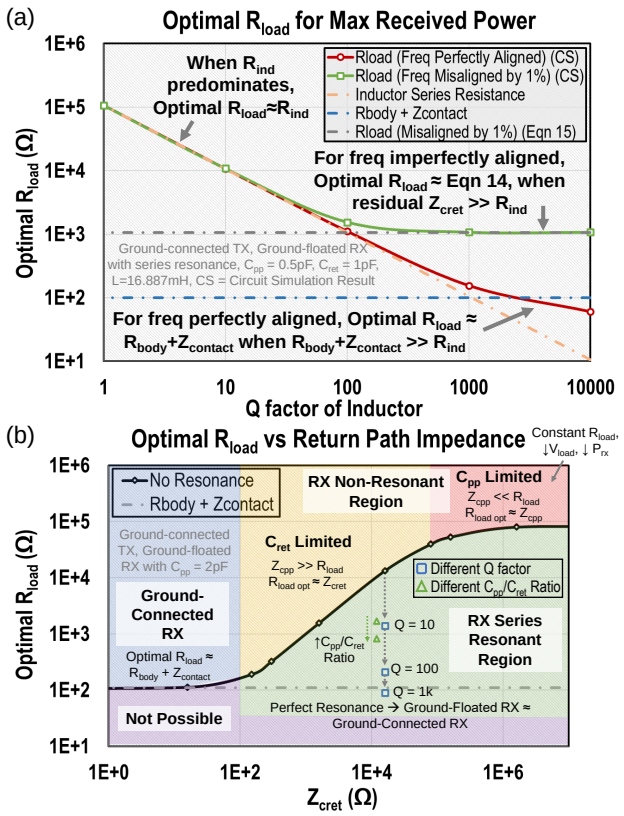

Fig. 12. (a) Optimal $\boldsymbol{R_{load}}$ that maximizes $\boldsymbol{P_{rx}}$ across two scenarios: perfect and imperfect frequency alignment between TX and RX series resonance frequency. (b) Optimal $\boldsymbol{R_{load}}$ that maximizes $\boldsymbol{P_{rx}}$ across different return path impedance, covering from ground-connected RX to ground-floated RX. This includes the series resonance improvement compared with no resonance.

of capacitive EQS-HBP. The four configurations can be effectively reduced to two primary cases: RX as either ground-floated or ground-connected, with TX ground-connected in both scenarios. As demonstrated earlier, resonance does not mitigate the effect of C_{ret} for a ground-floated TX. Consequently, the on-body voltage at the ground-floated TX contact point is determined solely by the ratio of $C_{ret\ TX}$ to C_{body} and remains unaffected by R_{body}, $Z_{contact}$, or the RX ground connection. Thus, the ground-floated TX can be modeled as a ground-connected TX with a reduced V_{tx}. Although ground-connected TX $Z_{contact}$ could vary V_{body} with different RX Z_{in}, ground-connected TX generally have much more relaxed sizing constraints compared to RX, leading to $Z_{contact\ TX} \ll R_{body}$, reducing the importance of this issue. Thus, we approximate $Z_{contact\ TX}$ as negligible.

For the configuration where both TX and RX are ground-connected, P_{rx} can be approximated as:

$$P_{rx} = \frac{1}{R_{load}} \cdot \left(V_{tx} \cdot \frac{R_{load}}{R_{load} + R_{body} + Z_{contact}} \right)^2 \quad (14)$$

In Eqn 14, maximum P_{rx} is achieved when $R_{load} = R_{body} + Z_{contact}$. Additionally, P_{rx} is inversely proportional to $R_{body} + Z_{contact}$, highlighting the importance of minimizing $Z_{contact}$ to enhance P_{rx}.

In the configuration where the RX is ground-floated and the TX is ground-connected with series resonance, resonance alignment and inductor Q factor significantly influence optimal R_{load}. When the RX resonant frequency aligns perfectly with the TX frequency, and the inductor Q factor is high with a large C_{ret}/C_{pp} ratio, C_{ret} can be effectively canceled, enabling $Z_{in} \approx R_{load}$. This transforms the ground-floated RX into a ground-connected configuration. As shown in Eqn 14, peak P_{rx} occurs when $R_{load} = R_{body} + Z_{contact}$, illustrated by the red curve in Fig 12(a) with an idealized Q factor approaching infinity.

However, when the inductor Q factor is low, as detailed in the previous subsection, the non-ideal inductor can be modeled as a perfect inductor in series with R_{ind}. While the ideal inductor cancels $Z_{C_{ret}}$, the RX Z_{in} becomes $R_{ind} + R_{load}$. If $R_{ind} \gg R_{body} + Z_{contact}$, then $Z_{in} \gg R_{body} + Z_{contact}$, and peak P_{rx} occurs when R_{load} matches R_{ind}, as shown in Fig 12(a) for low Q factor regions.

Practical misalignment between TX and RX frequencies further complicates performance. Minor frequency mismatches lead to incomplete cancellation of C_{ret}, and as the Q factor of a misaligned RX approaches infinity, RX $Z_{in} = R_{load} + Z_{C_{ret\ residual}}$. Since $Z_{C_{ret\ residual}} \gg R_{body} + Z_{contact}$ due to the small capacitance of C_{ret}, peak P_{rx} occurs when R_{load} matches $Z_{C_{ret\ residual}}$, calculable using parameters k_2–k_5 defined in Eqns 9–12:

$$R^2_{load\ opt} \approx \frac{k_3k_5 - 3k_2k_4 - \sqrt{(3k_2k_4 - k_3k_5)^2 - 4k_2k_3k_4k_5}}{2k_2k_5} \quad (15)$$

In summary, the optimal R_{load} for a ground-floated RX with series resonance can be expressed as:

$$R_{load\ opt} = \max(R_{ind}, R_{body} + Z_{contact}, Z_{C_{ret\ residual}}) \quad (16)$$

In the absence of resonance, P_{rx} can be approximated as:

$$P_{rx} = \frac{1}{Z_{load}} \cdot \left(V_{tx} \cdot \frac{Z_{load}}{Z_{load} + R_{body} + Z_{contact} + Z_{C_{ret}}} \right)^2 \quad (17)$$

As $Z_{C_{ret}} \gg R_{body} + Z_{contact}$, the denominator can be simplified to $Z_{load} + Z_{C_{ret}}$, where $Z_{load} = Z_{C_{pp}} || R_{load}$. When $C_{ret} \gg C_{pp}$, peak P_{rx} occurs at $R_{load} \approx Z_{C_{ret}}$ as $Z_{C_{pp}}$ can be disregarded, shown in Fig 12(b) in the C_{ret}-limited region. In contrast, when $C_{ret} \ll C_{pp}$, the peak P_{rx} occurs at $R_{load} \approx Z_{C_{pp}}$ as Z_{load} saturates with further R_{load} increment, shown in Fig 12(b) C_{pp}-limited region.

In summary, Fig 12(b) provides a comprehensive plot of this analysis. RX series resonance reduces the optimal R_{load}, with the extent of reduction primarily influenced by the inductor Q factor and the ratio of C_{ret} to C_{pp}. Given that the ratio of C_{ret} to C_{pp} varies less significantly than the inductor Q factor, optimizing the inductor Q factor is more critical. Additionally, $R_{body} + Z_{contact}$ sets a lower limit on the optimal R_{load}, highlighting the importance of minimizing $Z_{contact}$, as a lower optimal R_{load} typically leads to an increase in P_{rx}.

Finally, while Eqn 16 approximates R_{load} accurately in regions with clear maxima, it may not precisely predict R_{load} near the intersection of R_{ind} with either $R_{body} + Z_{contact}$ or $Z_{C_{ret\ residual}}$. Further research is needed to refine this. In practical applications, human motion introduces fluctuations in C_{ret} and C_{pp}, necessitating dynamic adjustments to the TX or RX resonant frequency to mitigate frequency misalignment and adjustments to R_{load} in response to these variations. This subsection, therefore, establishes approximate values and bounds for optimal R_{load}, providing a foundation for designing such an adaptive algorithm.

F. Key Takeaway

This section presents the theoretical framework for investigating the circuit theory behind the optimization of capacitive EQS-HBP. The major insights are:

- For a ground-floated RX

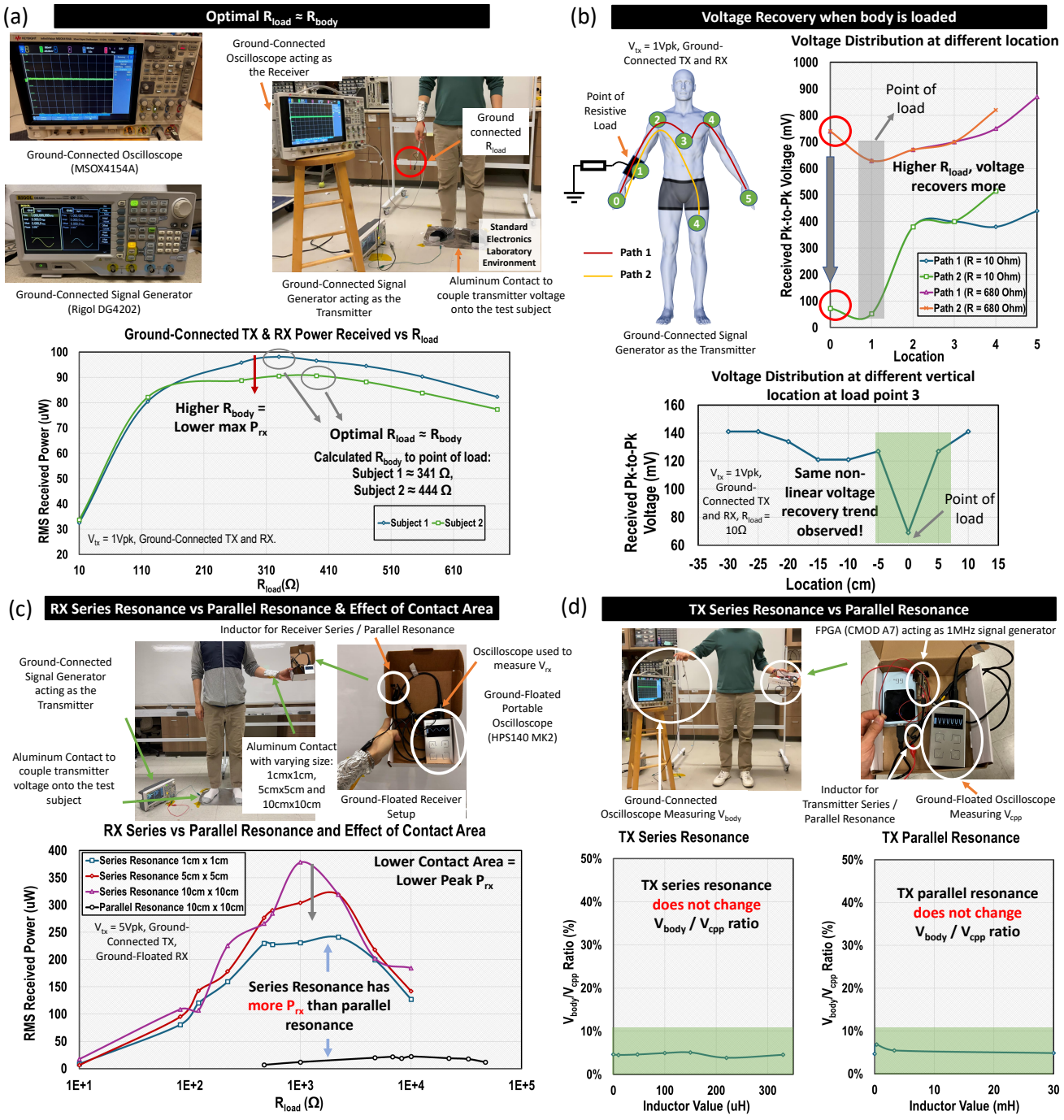

Fig. 13. (a) Experimental setup and results showing the optimal $\boldsymbol{R_{load} \approx R_{body}}$ when both TX and RX are ground-connected. (b) Experimental setup and voltage recovery trend when a body part connects to a low or a high $\boldsymbol{R_{load}}$ to ground. (c) Experimental setup and comparative results of RX series versus parallel resonance showing that series resonance has higher peak $\boldsymbol{P_{rx}}$ than parallel resonance and the impact of varying contact areas. (d) Experimental setup and analysis of TX series and parallel resonance, highlighting that neither will change the ratio of $\boldsymbol{V_{body}/V_{C_{pp}}}$.

  - Series resonance, compared with parallel resonance, is better at enhancing the P_{rx}
  - Series resonance will significantly reduce the Z_{in} from the body into the RX
  - The ratio between C_{pp} and C_{ret} and inductor Q factor determines the extent of the C_{ret} cancellation
  - An approximate to the optimal R_{load} for maximum P_{rx}
- For a ground-floated TX, series resonance could increase voltage coupling onto the body, but it is unable to cancel out the effect of C_{ret}
- Q factor significantly influences the P_{rx}. A higher Q factor will result in higher P_{rx} across all configurations with resonance.

VII. Physical Experiment

To validate the theoretical investigation and simulations conducted in HFSS, four in-vivo experiments were performed in a laboratory environment with the setup and result presented in Fig 13.

A. Experiment Safety

The study was approved by the Purdue Institutional Review Board (IRB Protocol no. IRB-2022-1681), and all guidelines and regulations stipulated by the Purdue IRB were followed. Informed consent was obtained from participants prior to the experiments. Extensive simulation in HFSS with regard to maximum E-field, H-Field, and

specific absorption rate (SAR) inside the body is conducted to ensure they are within the guidelines of the International Commission on Non-Ionizing Radiation Protection (ICNIRP) [40].

B. Experiment Result

In Fig 13(a), an experiment was conducted to validate the simulation from section IV. Two participants with similar height (170cm) but differing weights were involved. The same setup was used for both participants: a ground-connected signal generator served as the TX to couple a 1Vpp, 1MHz sine wave onto the body. A ground-connected oscilloscope, with its ground also connected to that of the signal generator, measured V_{rx} across R_{load}. One end of R_{load} was connected to the body through a large aluminum wrap on the arm, while the other end was grounded. Despite having equal height, subject 2, being leaner than subject 1, exhibited a higher R_{body}, resulting in a lower maximum P_{rx}. This finding supports the conclusion in section IV, indicating that R_{body} can be approximated by Eqn 1 and, with minimal contact impedance, the optimal $R_{load} \approx R_{body}$.

In Fig 13(b), an experiment was conducted to validate the simulation from section V using subject 1, with an identical setup as in (a) except for the load point location. The results show that when a small R_{load} is attached to the body, the on-body voltage can recover around the load point on the torso but fails to recover at the fingertip, which is beyond the load point on the arm. Additionally, with a higher R_{load}, the on-body voltage at the fingertip recovers to the rest of the on-body voltage compared to when the R_{load} is lower, the on-body voltage at the fingertip is unable to recover. This finding supports the conclusion in section V, indicating that on-body voltage recovery after the load point depends on both the cross-sectional area of the body region in contact and the R_{load}.

In Fig 13(c), an experiment was conducted to validate the simulation from section IV and VI using subject 1, with the setup illustrated in (d). The experiment aimed to confirm that series resonance is preferable to parallel resonance for RX and to demonstrate the impact of $Z_{contact}$. A ground-connected signal generator served as the TX, coupling a 5Vpk, 1MHz sine wave onto the body. A ground-floated RX setup was also used, with an inductor configured for series or parallel resonance and a portable oscilloscope measuring the received voltage across the resistor. For series resonance, a 1mH inductor was used with three different contact areas: 1cm x 1cm, 5cm x 5cm, and 10cm x 10cm. For parallel resonance, a 220uH inductor with a 10cm x 10cm contact area was used. The results show that series resonance achieves significantly greater P_{rx} than parallel resonance, and a larger contact area further enhances P_{rx}. This finding supports the conclusions in sections IV and VI, indicating that for capacitive EQS-HBP, RX benefits more from a series resonance configuration than from parallel resonance, and a larger contact area minimizes $Z_{contact}$ for improved P_{rx}. Additionally, due to non-idealities associated with the inductor, the observed improvement ratio between series and parallel resonance exceeds that in the simulation.

In Fig 13(d), an experiment was conducted to validate the simulation from section VI using subject 1, with the setup illustrated in (d). This experiment aimed to confirm that, for capacitive EQS-HBP TX, neither series nor parallel resonance techniques can cancel the effect of C_{ret} and thus cannot alter the ratio between $V_{C_{pp}}$ and V_{body}. An FPGA served as the ground-floated TX, coupling a 5Vpk, 1MHz square wave onto the body, with an inductor used for series or parallel resonance. A portable oscilloscope measured the voltage across the parasitic capacitor C_{pp}, while a ground-connected oscilloscope measured the on-body voltage. The results demonstrate a consistent ratio between $V_{C_{pp}}$ and V_{body} for both TX series and parallel resonance configurations, validating the conclusion that inductive resonance does not cancel the effect of C_{ret} for the TX.

In these experiments, the focus is to validate the biophysical modeling results and trends and not on maximizing the absolute P_{rx} or exact number matching between simulation and experiment. With more optimization from the device form factor and location, it is possible to achieve mW level power, and a specific modality with $> 2mW$ has been shown by Datta et al. [8]. To increase the P_{rx}, an inductor with a higher quality factor should be used (in this experiment, a generic commonly found in electronics laboratory inductor is used). Future research should focus on optimizing resonance alignment to enhance resonance efficiency, refining device form factors to improve electrode size (affecting $Z_{contact}$) and ground size (impacting C_{pp} and C_{ret}), and optimizing the device location to further optimize the magnitude of C_{pp} and C_{ret}.

VIII. Summary of Key Findings and Discussion

This paper has investigated capacitive EQS-HBP from two perspectives: biophysical modeling and circuit optimization.

For biophysical modeling, the body channel is modeled as a uniformly distributed R_{body}, which is a function of the bulk conductivity and the body dimension. Using that, the V_{body} across different locations could be found using Eqn 2. As R_{load} maximizing P_{rx} exists in the range of $Z_{contact}$, a second element is added to model that effect. It is found that $Z_{contact}$ has an inverse relationship to the contact area, and for wearables, it is advised to have a minimal contact area of $1cm^2$. With R_{body} and $Z_{contact}$, a lumped circuit model for capacitive EQS-HBP is developed. Fig 14(a) shows increasing $Z_{contact}$ or R_{body} decreases P_{rx} across four modes of capacitive EQS-HBP. Furthermore, V_{body} can be approximated as equipotential when RX $Z_{in} \gg R_{body} + Z_{contact}$ (high impedance termination for capacitive EQS-HBC) but to impedance matching between Z_{in}, R_{load} and $R_{body} + Z_{contact}$ is required maximize P_{rx}. Lastly, an analysis was performed to investigate how the body cross-sectional area would reduce on-body voltage recovery after the low impedance loading point, and this provides guidance for device placement optimization.

For circuit optimization, we have proved that using series resonance is the most effective at boosting P_{rx} for both ground-floated TX and RX. Furthermore, series resonance is able to cancel out the effect of C_{ret} for the ground-floated RX but is unable to cancel out the effect of C_{ret} for the TX. We have found that decreasing the ratio between C_{pp}/C_{ret} helps with increasing the P_{rx}, and Fig 14 (b) and (c) shows the effect of that. Reducing the ratio of C_{pp}/C_{ret} for a ground-connected TX and ground-floated RX boosts the P_{rx} but is less effective in boosting P_{rx} than having series resonance from both the ground-floated TX and ground-floated RX. Fig 14(c) contains the result of two phenomenons: TX series resonance boosting V_{body} and increasing C_{ret} reducing the capacitive division of $V_{body}/V_{C_{pp}}$. Thus, practical design should boost TX C_{ret} while doing series resonance to gain the most benefit. Fig 14(d) shows the potential of using series resonance on both the TX and the RX, with the given setup, 2.5Vpk input could achieve more than 400uW of P_{rx} with 3pF of C_{ret} and 2pF of C_{pp}. However, aligning resonance between the TX and the RX is difficult, and slight misalignment could significantly reduce the P_{rx}, as shown in Fig 14(e). Future research is required to generate solutions to ensure TX and RX alignment automatically. Fig 14(f) shows the impact of TX source impedance on P_{rx}, and for practical application, keeping R_{src} low will boost the P_{rx}. A closed-formed equation (eqn 15) has been developed to predict the optimal R_{load} for a ground-floated RX design for maximizing the P_{rx}. Lastly, the effect of the Q factor

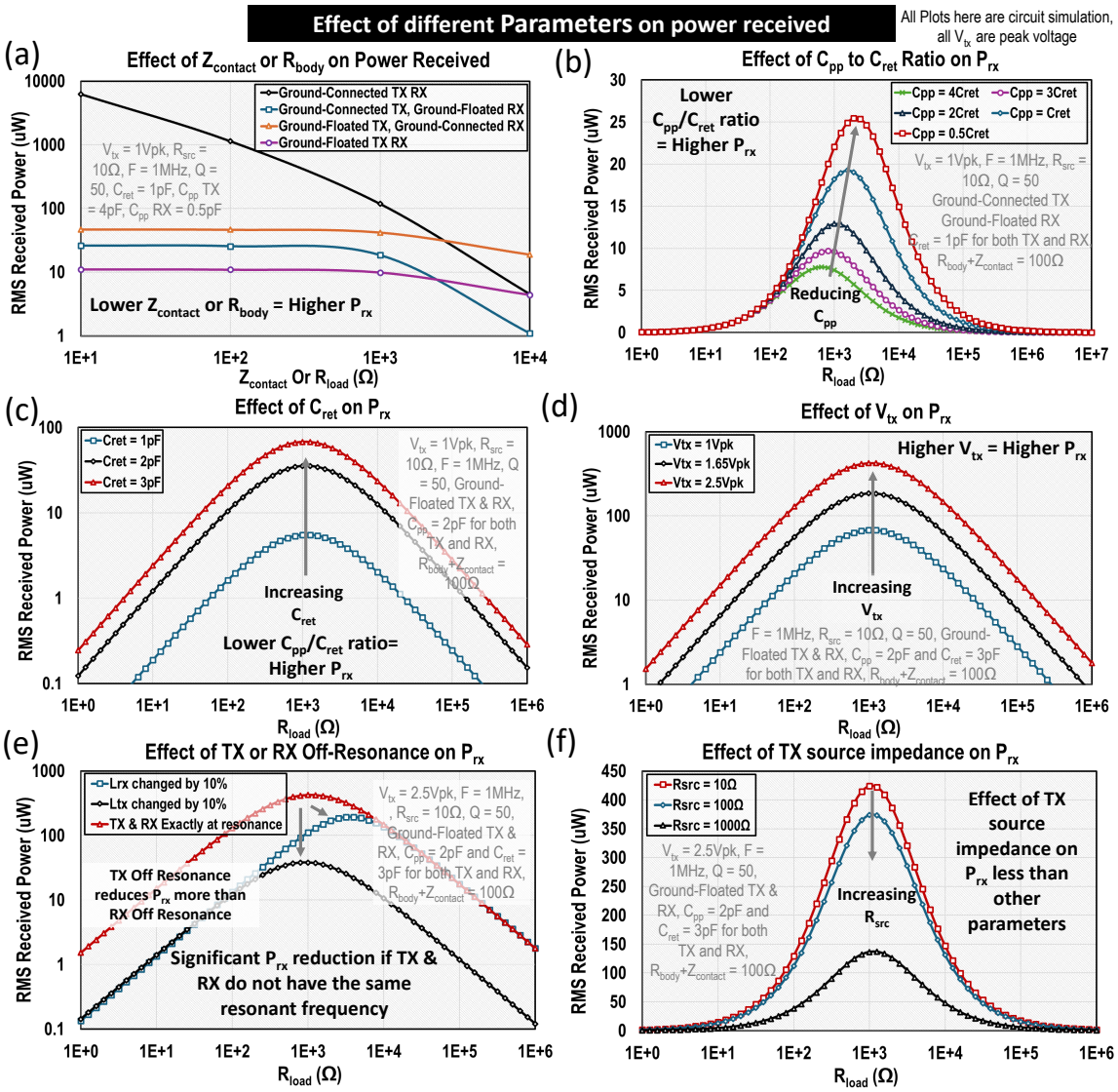

Fig. 14. (a) shows how changing $\boldsymbol{Z_{contact}}$ or $\boldsymbol{R_{body}}$ affects $\boldsymbol{P_{rx}}$ for four different capacitive EQS-HBP configurations. (b) shows how the ratio of $\boldsymbol{C_{pp}/C_{ret}}$ affects the $\boldsymbol{P_{rx}}$ for a ground-connected TX and ground-floated RX system. (c) shows the effect of reducing the ratio of $\boldsymbol{C_{pp}/C_{ret}}$ on the $\boldsymbol{P_{rx}}$ for a ground-floated TX & RX system. (d) shows the effect of $\boldsymbol{V_{tx}}$ on the $\boldsymbol{P_{rx}}$ for a ground-floated TX and RX system. (e) shows how off-resonance at either the TX or RX affects the $\boldsymbol{P_{rx}}$ for a ground-floated TX and RX system. (f) shows the effect of TX source impedance on the $\boldsymbol{P_{rx}}$ for a ground-floated TX and RX system. All simulations assume constant on-body location and contact area. Effects of changing on-body location and contact area can be found in Fig 4(f) and Fig 5(e).

on the P_{rx} has been analyzed through circuit simulation, and we found that increasing the Q factor will increase the P_{rx} across the different configurations of capacitive EQS-HBP.

IX. Conclusion

The capacitive EQS-HBP method demonstrates significant potential for enhancing power delivery by confining the signal within the body rather than radiating it outward. This study presents, for the first time, a theoretical model grounded in biophysics to elucidate the fundamental mechanisms and constraints governing power transfer in capacitive EQS-HBP. The analysis identifies the critical roles of R_{body} and $Z_{contact}$ in determining power delivery, highlighting scenarios where these factors become pivotal or negligible. Additionally, the research pioneers the application of series resonance to effectively mitigate C_{ret}, achieving substantial improvements in P_{rx} on the RX side. The findings also quantify power delivery performance across various scenarios, providing actionable insights into optimizing system parameters for different use cases. The comprehensive analysis reveals the influence of body dimensions, contact area, and cross-sectional area on power recovery, offering practical design guidance. These results underscore the importance of tailoring system designs to specific device and application requirements. Beyond technical contributions, this work has significant implications for advancing wearable body area networks (WBANs) and IoB systems. By addressing critical challenges limiting consistent and high wireless power delivery, capacitive EQS-HBP opens avenues for more reliable and efficient powering of next-generation wearable technologies. This study thus establishes a foundational framework for further exploration and innovation in the field of wearable power transfer systems.

X. Acknowledgements

This work was supported by Quasistatics, Inc. - Grant 40003567. Account F.00127126.02.036. The authors thank Samyadip Sarkar and David Yang, PhD students at SparcLab, for their valuable input during the experiment and discussion process.

REFERENCES

[1] A. Datta and S. Sen, "Invited: IoB: The Vision of the Internet of Bodies," *Midwest Symposium on Circuits and Systems*, pp. 444–448, 2023.

[2] H. C. Ates, C. Ates, and C. Dincer, "Stress monitoring with wearable technology and AI," *Nature Electronics 2024 7:2*, vol. 7, no. 2, pp. 98–99, 2 2024. [Online]. Available: https://www.nature.com/articles/s41928-024-01128-w

[3] V. Ricotti, B. Kadirvelu, V. Selby *et al.*, "Wearable full-body motion tracking of activities of daily living predicts disease trajectory in Duchenne muscular dystrophy," *Nature Medicine 2023 29:1*, vol. 29, no. 1, pp. 95–103, 1 2023. [Online]. Available: https://www.nature.com/articles/s41591-022-02045-1

[4] K. K. Balasubramanian, A. Merello, G. Zini *et al.*, "Neural network-based Bluetooth synchronization of multiple wearable devices," *Nature Communications 2023 14:1*, vol. 14, no. 1, pp. 1–10, 7 2023. [Online]. Available: https://www.nature.com/articles/s41467-023-40114-2

[5] S. Sen, S. Maity, and D. Das, "The body is the network: To safeguard sensitive data, turn flesh and tissue into a secure wireless channel," *IEEE Spectrum*, vol. 57, no. 12, pp. 44–49, 12 2020.

[6] N. Modak, D. Das, M. Nath *et al.*, "EQS Res-HBC: A 65-nm Electro-Quasistatic Resonant 5-240 μw Human Whole-Body Powering and 2.19 μw Communication SoC with Automatic Maximum Resonant Power Tracking," *IEEE Journal of Solid-State Circuits*, vol. 57, no. 3, pp. 831–844, 3 2022.

[7] J. Li, Y. Dong, J. H. Park *et al.*, "Body-coupled power transmission and energy harvesting," *Nature Electronics 2021 4:7*, vol. 4, no. 7, pp. 530–538, 6 2021. [Online]. Available: https://www.nature.com/articles/s41928-021-00592-y

[8] A. Datta, L. Ding, and S. Sen, "Step-to-Charge: mW-scale power transfer to on-body devices for long channel ($>$ 1m) with EQS Resonant Human Body Powering," 8 2024. [Online]. Available: https://arxiv.org/abs/2408.01927v1

[9] H. Cho, J. H. Suh, C. Kim *et al.*, "An Intra-Body Power Transfer System with $>$1-mW Power Delivered to the Load and 3.3-V DC Output at 160-cm of on-Body Distance," *IEEE Transactions on Biomedical Circuits and Systems*, vol. 16, no. 5, pp. 852–866, 10 2022.

[10] S. Maity, M. He, M. Nath *et al.*, "Bio-Physical Modeling, Characterization, and Optimization of Electro-Quasistatic Human Body Communication," *IEEE Transactions on Biomedical Engineering*, vol. 66, no. 6, pp. 1761–1802, 6 2019.

[11] S. Gabriel, R. W. Lau, and C. Gabriel, "The dielectric properties of biological tissues: III. Parametric models for the dielectric spectrum of tissues," *Physics in Medicine & Biology*, vol. 41, no. 11, p. 2271, 11 1996. [Online]. Available: https://iopscience.iop.org/article/10.1088/0031-9155/41/11/003 https://iopscience.iop.org/article/10.1088/0031-9155/41/11/003/meta

[12] A. Datta, M. Nath, D. Yang *et al.*, "Advanced Biophysical Model to Capture Channel Variability for EQS Capacitive HBC," *IEEE Transactions on Biomedical Engineering*, vol. 68, no. 11, pp. 3435–3446, 11 2021.

[13] N. Cho, J. Yoo, S. J. Song *et al.*, "The human body characteristics as a signal transmission medium for intrabody communication," *IEEE Transactions on Microwave Theory and Techniques*, vol. 55, no. 5, pp. 1080–1085, 2007.

[14] S. Maity, M. Nath, G. Bhattacharya *et al.*, "On the Safety of Human Body Communication," *IEEE Transactions on Biomedical Engineering*, vol. 67, no. 12, pp. 3392–3402, 12 2020.

[15] M. Nath, S. Maity, and S. Sen, "Toward Understanding the Return Path Capacitance in Capacitive Human Body Communication," *IEEE Transactions on Circuits and Systems II: Express Briefs*, vol. 67, no. 10, pp. 1879–1883, 10 2020.

[16] S. Maity, K. Mojabe, and S. Sen, "Characterization of Human Body Forward Path Loss and Variability Effects in Voltage-Mode HBC," *IEEE Microwave and Wireless Components Letters*, vol. 28, no. 3, pp. 266–268, 3 2018.

[17] J. Park, H. Garudadri, and P. P. Mercier, "Channel Modeling of Miniaturized Battery-Powered Capacitive Human Body Communication Systems," *IEEE Transactions on Biomedical Engineering*, vol. 64, no. 2, pp. 452–462, 2 2017.

[18] X. Q. Zhu, Y. X. Guo, and W. Wu, "Investigation and Modeling of Capacitive Human Body Communication," *IEEE Transactions on Biomedical Circuits and Systems*, vol. 11, no. 2, pp. 474–482, 4 2017.

[19] W. C. Wang, Z. D. Nie, F. Guan *et al.*, "Experimental studies on human body communication characteristics based upon capacitive coupling," *Proceedings - 2011 International Conference on Body Sensor Networks, BSN 2011*, pp. 180–185, 2011.

[20] Y. Nishida, K. Sasaki, K. Yamamoto *et al.*, "Equivalent Circuit Model Viewed from Receiver Side in Human Body Communication," *IEEE Transactions on Biomedical Circuits and Systems*, vol. 13, no. 4, pp. 746–755, 8 2019.

[21] J. Mao, H. Yang, Y. Lian *et al.*, "Channel Loss in Contactless Human Body Communication," *Proceedings of the Annual International Conference of the IEEE Engineering in Medicine and Biology Society, EMBS*, vol. 2018-July, pp. 3762–3765, 10 2018.

[22] J. H. Hwang, J. B. Sung, S. E. Kim *et al.*, "Effect of load impedance on the signal loss of human body communication," *IEEE Antennas and Propagation Society, AP-S International Symposium (Digest)*, pp. 3217–3220, 2007.

[23] Y. Zhang, Z. He, Y. Liu *et al.*, "Measurement and characterization on a human body communication channel," *IEEE International Symposium on Personal, Indoor and Mobile Radio Communications, PIMRC*, 12 2016.

[24] T. W. Kang, J. H. Hwang, C. H. Hyoung *et al.*, "Performance evaluation of human body communication system for IEEE 802.15 on the effect of human body channel," *Proceedings of the International Symposium on Consumer Electronics, ISCE*, pp. 232–235, 2011.

[25] S. Maity, B. Chatterjee, G. Chang *et al.*, "BodyWire: A 6.3-pJ/b 30-Mb/s-30-dB SIR-Tolerant Broadband Interference-Robust Human Body Communication Transceiver Using Time Domain Interference Rejection," *IEEE Journal of Solid-State Circuits*, vol. 54, no. 10, pp. 2892–2906, 10 2019.

[26] D. Das, S. Maity, B. Chatterjee *et al.*, "Enabling Covert Body Area Network using Electro-Quasistatic Human Body Communication," *Scientific Reports*, vol. 9, no. 1, 12 2019.

[27] S. Maity, D. Das, and S. Sen, "Wearable health monitoring using capacitive voltage-mode Human Body Communication," *Proceedings of the Annual International Conference of the IEEE Engineering in Medicine and Biology Society, EMBS*, pp. 1–4, 9 2017.

[28] N. Modak, M. Nath, B. Chatterjee *et al.*, "Bio-Physical Modeling of Galvanic Human Body Communication in Electro-Quasistatic Regime," *IEEE Transactions on Biomedical Engineering*, vol. 69, no. 12, pp. 3717–3727, 12 2022.

[29] J. Li, Y. Dong, L. Lin *et al.*, "Concurrent Body-Coupled Powering and Communication ICs With a Single Electrode," *IEEE Journal of Solid-State Circuits*, vol. 59, no. 4, pp. 1006–1016, 4 2024.

[30] J. Li, Y. Dong, L. Lin *et al.*, "Wireless Body-Area Network Transceiver ICs with Concurrent Body-Coupled Powering and Communication using Single Electrode," *Digest of Technical Papers - Symposium on VLSI Technology*, vol. 2023-June, 2023.

[31] Y. Zhu, J. Y. Fong, L. Lin *et al.*, "Biomedical System-on-Chip Design with Integrated Body-Coupled Powering," *BioCAS 2023 - 2023 IEEE Biomedical Circuits and Systems Conference, Conference Proceedings*, 2023.

[32] J. Yoo, "Body Area Network: Connecting and powering things together around the human body," *IEEE Solid-State Circuits Magazine*, vol. 15, no. 2, pp. 49–58, 3 2023.

[33] J. Li and J. Yoo, "Body-Coupled Powering for Wearables," *RFIT 2022 - 2022 IEEE International Symposium on Radio-Frequency Integration Technology*, pp. 38–39, 2022.

[34] J. Li, Y. Dong, J. H. Park *et al.*, "Body-coupled power transmission and energy harvesting," *Nature Electronics 2021 4:7*, vol. 4, no. 7, pp. 530–538, 6 2021. [Online]. Available: https://www.nature.com/articles/s41928-021-00592-y

[35] Y. Dong, J. Li, L. Lin *et al.*, "Body-Coupled Power Transceiver with Node-Specific Body-Area Powering," *ESSCIRC 2021 - IEEE 47th European Solid State Circuits Conference, Proceedings*, pp. 423–426, 9 2021.

[36] J. Li, Y. Dong, J. H. Park *et al.*, "Body-Area Powering with Human Body-Coupled Power Transmission and Energy Harvesting ICs," *IEEE Transactions on Biomedical Circuits and Systems*, vol. 14, no. 6, pp. 1263–1273, 12 2020.

[37] J. Li, Y. Dong, J. H. Park *et al.*, "Human-Body-Coupled Power-Delivery and Ambient-Energy-Harvesting ICs for a Full-Body-Area Power Sustainability," *Digest of Technical Papers - IEEE International Solid-State Circuits Conference*, vol. 2020-February, pp. 514–516, 2 2020.

[38] J. Lee, Y. Lee, H. Cho *et al.*, "A 48 μw, 8.88 × 10-3 W/W batteryless energy harvesting BCC identification system," *Proceedings - IEEE International Symposium on Circuits and Systems*, vol. 2016-July, pp. 1806–1809, 7 2016.

[39] S. Maity, M. He, M. Nath *et al.*, "Bio-Physical Modeling, Characterization, and Optimization of Electro-Quasistatic Human Body Communication," *IEEE Transactions on Biomedical Engineering*, vol. 66, no. 6, pp. 1761–1802, 6 2019.

[40] G. Ziegelberger, R. Croft, M. Feychting *et al.*, "Guidelines for limiting exposure to electromagnetic fields (100 kHz to 300 GHz)," pp. 483–524, 5 2020.

APPENDIX I
DERIVATION FOR $Z_{in}, P_{R_{load}}$ AND R_{load}

$$Z_{\text{in}} = \left(\frac{1}{\frac{1}{Z_{C_{pp}}} + \frac{1}{Z_L + R_{\text{load}}}} \right) + Z_{C_{\text{ret}}}$$

$$Z_{\text{in}} = \frac{Z_{C_{pp}} * (Z_L + R_{\text{load}})}{Z_{C_{pp}} + Z_L + R_{\text{load}}} + Z_{C_{\text{ret}}}$$

$$Z_{\text{in}} = \frac{Z_{C_{pp}} (Z_L + R_{\text{load}}) + Z_{C_{\text{ret}}} \left(Z_{C_{pp}} + Z_L + R_{\text{load}} \right)}{Z_{C_{pp}} + Z_L + R_{\text{load}}}$$

$$Z_{\text{in}} = \frac{Z_L + R_{\text{load}} + \frac{Z_{C_{\text{ret}}}}{Z_{C_{pp}}} \left(Z_{C_{pp}} + Z_L + R_{\text{load}} \right)}{1 + \frac{1}{Z_{C_{pp}}} (Z_L + R_{\text{load}})}$$

$$Z_{\text{in}} = \frac{Z_L + R_{\text{load}} + Z_{C_{\text{ret}}} + \frac{Z_{C_{\text{ret}}}}{Z_{C_{pp}}} (Z_L + R_{\text{load}})}{1 + \frac{1}{Z_{C_{pp}}} (Z_L + R_{\text{load}})}$$

$$Z_{\text{in}} = \frac{Z_L + R_{\text{load}} + \frac{1}{SC_{\text{ret}}} + \frac{C_{pp}}{C_{\text{ret}}} (Z_L + R_{\text{load}})}{1 + SC_{pp} (Z_L + R_{\text{load}})}$$

$$Z_{\text{in}} = \frac{\frac{1}{SC_{ret}} + \left(1 + \frac{C_{pp}}{C_{ret}} \right) (Z_L + R_{\text{load}})}{1 + SC_{pp} (Z_L + R_{\text{load}})}$$

$$Z_{\text{in}} = \frac{\frac{1}{SC_{ret}} + \left(\frac{C_{ret} + C_{pp}}{C_{\text{ret}}} \right) (Z_L + R_{\text{load}})}{1 + SC_{pp} (Z_L + R_{\text{load}})}$$

$$Z_{\text{in}} = \frac{\frac{1}{SC_{\text{ret}}} + \left(\frac{C_{\text{ret}} + C_{pp}}{C_{\text{ret}}} \right) (SL + R_{\text{load}})}{1 + SC_{pp} (SL + R_{\text{load}})}$$

$$Z_{\text{in}} = \frac{1 + S (C_{ret} + C_{pp}) (SL + R_{\text{load}})}{SC_{\text{ret}} + S^2 C_{pp} C_{\text{ret}} (SL + R_{\text{load}})}$$

$$Z_{\text{in}} = \frac{1 + (C_{ret} + C_{pp}) S^2 L + S (C_{ret} + C_{pp}) R_{\text{load}}}{SC_{ret} + S^3 C_{pp} C_{ret} L + S^2 C_{pp} C_{ret} R_{\text{load}}}$$

$$Z_{\text{in}} = \frac{1 - (C_{ret} + C_{pp}) L\omega^2 + j (C_{ret} + C_{pp}) R_{\text{load}} \omega}{j\omega C_{ret} - j\omega^3 C_{pp} C_{ret} L - \omega^2 C_{pp} C_{ret} R_{\text{load}}}$$

$$Z_{\text{in}} = \frac{1 - (C_{ret} + C_{pp}) L\omega^2 + j (C_{ret} + C_{pp}) R_{\text{load}} \omega}{-\omega^2 C_{pp} C_{ret} R_{\text{load}} + j (\omega C_{ret} - \omega^3 C_{pp} C_{\text{ret}} L)}$$

$$|Z_{\text{in}}| = \frac{\sqrt{[1 - (C_{ret} + C_{pp}) L\omega^2]^2 + [(C_{ret} + C_{pp}) R_{\text{load}} \omega]^2}}{\sqrt{(\omega^2 C_{pp} C_{ret} R_{\text{load}})^2 + (\omega C_{ret} - \omega^3 C_{pp} C_{ret} L)^2}}$$

$$|Z_{\text{in}}| = \frac{\sqrt{[1 - (C_{ret} + C_{pp}) L\omega^2]^2 + [(C_{ret} + C_{pp}) \omega]^2 R_{\text{load}}^2}}{\sqrt{(\omega^2 C_{pp} C_{ret})^2 R_{\text{load}}^2 + (\omega C_{ret} - \omega^3 C_{pp} C_{ret} L)^2}}$$

To simplify:

$$k_2 = \left(\omega^2 C_{pp} C_{ret} \right)^2$$

$$k_3 = \left(\omega C_{ret} - \omega^3 C_{pp} C_{ret} L \right)^2$$

$$k_4 = \left[1 - (C_{ret} + C_{pp}) L\omega^2 \right]^2$$

$$k_5 = [(C_{ret} + C_{pp}) \omega]^2$$

Thus:

$$|Z_{\text{in}}| = \sqrt{\frac{k_4 + k_5 R_{\text{load}}^2}{k_2 R_{\text{load}}^2 + k_3}}$$

$$P_{R_{\text{load}}} = \left(\frac{C_{pp} + C_{\text{ret}}}{C_{\text{ret}}} \frac{V_{\text{body}}}{Z_{\text{in}}}\right)^2 R_{\text{load}}$$

$$P_{R_{\text{load}}} = \left(\frac{C_{pp} + C_{\text{ret}}}{C_{\text{ret}}} * V_{\text{body}}\right)^2 * \frac{k_2 R_{\text{load}}^2 + k_3}{k_4 + k_5 R_{\text{load}}^2} * R_{\text{load}}$$

To simplify:

$$k_1 = \left(\frac{C_{pp} + C_{\text{ret}}}{C_{\text{ret}}} * V_{\text{body}}\right)^2$$

$$P_{R_{\text{load}}} = k_1 * \frac{k_2 R_{\text{load}}^2 + k_3}{k_4 + k_5 R_{\text{load}}^2} * R_{\text{load}}$$

To find local maxima where power is maximized with respect to R_{load}:

$$\frac{dP_{R_{\text{load}}}}{dR_{\text{load}}} = \frac{1}{dR_{\text{load}}}\left(k_1 * \frac{k_2 R_{\text{load}}^2 + k_3}{k_4 + k_5 R_{\text{load}}^2} * R_{\text{load}}\right) = 0$$

$$\frac{1}{dR_{load}}\left(k_1\left(\frac{k_2 R_{load}^3 + k_3 R_{load}}{k_4 + k_5 R_{load}^2}\right)\right)$$

$$= \frac{k_1}{(k_4 + k_5 R_{load}^2)^2}[(k_4 + k_5 R_{load}^2)(3k_2 R_{load}^2 + k_3) - (k_2 R_{load}^3 + k_3 R_{load})(2k_5 R_{load})]$$

Thus,

$$(k_4 + k_5 R_{load}^2)(3k_2 R_{load}^2 + k_3) - (k_2 R_{load}^3 + k_3 R_{load})(2k_5 R_{load})$$

$$= R_{load}^4(k_2 k_5) + R_{load}^2(3k_2 k_4 - k_3 k_5) + k_3 k_4 = 0$$

$$R_{load}^2 = \frac{-(3k_2 k_4 - k_3 k_5 \pm \sqrt{(3k_2 k_4 - k_3 k_5)^2 - 4 * k_2 k_3 k_4 k_5}}{2 * k_2 k_5}$$

$$= \frac{k_3 k_5 - 3k_2 k_4 - \sqrt{(3k_2 k_4 - k_3 k_5)^2 - 4k_2 k_3 k_4 k_5}}{2k_2 k_5}$$